

Comparative Planetary Circulation Regimes with a Simplified GCM

DPhil 2nd Year Report

Yixiong Wang

Atmospheric, Oceanic and Planetary Physics
Department of Physics

St Cross College

University of Oxford

Supervisor: Professor Peter Read

Word count: ~11000

Abstract

This report presents the second year's work of my DPhil project. The overall objective of this project is to establish a parameter space in which the dependence of terrestrial planetary circulation regimes are mapped with respect to defining dimensionless parameters. In this report, a brief summary of the first year's work on varying the planetary rotation rate is presented. A 1-D semi-grey radiative-convective (R-C) model is constructed and validated against the analytical grey atmosphere model. The model is shown to be able to reproduce the fundamental structures of rocky planetary atmospheres like that of Mars and the Earth. A programme calculating the incoming stellar radiation (ISR) at top of atmosphere (TOA) for different latitudes is developed and coupled with this 1-D R-C model so that the 1-D model could run at various latitudes to simulate meridional variations of temperature. Effects of changing values of three radiative parameters (planetary obliquity, total optical depth of long-wave band, and the ratio of long-wave to shortwave optical depths) are investigated. Future work will couple the simplified 1-D R-C scheme to the 3-D PUMA model and run ensemble experiments by varying different dimensionless parameters.

Contents

1	Introduction	1
1.1	The problem	1
1.2	Dimensionless parameters for planetary circulation	6
1.3	Chapter introductions	8
2	First Year Summary and Overview of Second Year	9
2.1	Summary of first year's work	9
2.2	Second year's work—overview and justification	12
2.2.1	Overview	12
2.2.2	Justification	12
3	1-D Radiative-Convective Model	15
3.1	Radiative transfer	15
3.2	Convective adjustment	20
3.3	Vertical discretisation	21
4	Model Validation	22
4.1	Grey atmosphere validation	22
4.2	Modelling Earth's atmosphere	24
4.3	Modelling Martian atmosphere	28
5	Extended 1-D R-C Model with Latitudinal Variations	32
5.1	Incoming stellar radiation (ISR) at top of atmosphere for different latitudes	32
5.2	Using ISR as an external forcing of the 1-D R-C model	34
6	Glimpse of the Radiative Parameter Space	40
6.1	Choose of parameters	40
6.2	Sensitivity of global average thermal structure	41
6.3	Sensitivity of the equator-to-pole temperature difference	44

7	Conclusions and Future Work	48
7.1	Major conclusions	48
7.2	Discussions and future plan	49
7.2.1	Dimensionless parameters	49
7.2.2	$\Delta\theta_h$ parametrisation revisited	50
7.2.3	Time plan	51

Chapter 1

Introduction

I think the Causes of the General Trade-Winds have not been fully explained by any of those who have wrote on that Subject...

— George Hadley (1735)

1.1 The problem

There has long been various attempts to reveal the fundamental mechanism of the atmospheric general circulation in history, proposing fairly diverse driving forces (see the review by Lorenz (1969)). The first scientifically serious and physically solid work, however, is Hadley's seminal paper in 1735 (Hadley (1735)). In this pathbreaking paper, Hadley correctly pointed out that the Earth's rotational effect should be taken into consideration to achieve a sound explanation of the distribution of general trade winds in the tropics. By noticing this rotational effect, combined with the observational fact of temperature difference between the equator and the poles, he finally came up with a global axisymmetric overturning circulation which applies not just to the tropical regions. In his purely qualitative arguments, Hadley filters the influences of various irregular factors by assuming that they only play a marginal role in determining the circulation regime, and that the real circulation pattern only differs to some extent from the conceived ideal atmosphere. He neglected the influence of diurnal and seasonal cycles of insolation, the thermal irregularities caused by continents and oceans, the topographical effect of mountains, and the thermodynamic effect of water vapour. The only constraints reserved for his investigation are planetary rotation and the annual mean meridional temperature gradient. This philosophy of abstracting the planetary atmosphere as a rotating fluid system

under inhomogeneous thermal forcing shapes the standard paradigm of the following centuries’ study of atmospheric general circulation (and perhaps other geophysical fluid systems as well).

Development in planetary circulation study thereafter follows roughly the same procedure with many other subjects in physics. Simplified ideal models, modified continuously by observations, were extensively designed and studied by theoreticians (Ferrel (1889), Thomson (1892)), which eventually leads to the modern 3-cell circulation model. On the other hand, laboratory techniques greatly progressed in the 20th century and enabled the investigation of rotating fluids through laboratory experiments (Fultz et al. (1959), Hide (1953)). One of these laboratory settings that bear significant resemblance to atmospheric circulation is the rotating annulus, which was originally designed by Raymond Hide to study the Earth’s mantle flow (Hide (2010)). The typical configuration of a rotating annulus is shown in Figure 1.1. If its inner cylinder is cooled and the outer cylinder heated, then such configuration of rotating fluids essentially captures the key physics of planetary atmospheric circulation: that is, rotating fluids driven by the forcing of differential stellar heating. This greatly simplifies the realistic atmosphere and bestows upon the experimenter the ease of gaining insights of a complex system by studying its laboratory analogue, which has more regular geometry and external forcings, but less physical processes of marginal importance (e.g. topography, latent heat of phase change, chemistry and so on).

A natural question when studying the rotating annulus is that what is the defining parameters, amongst a series of physical parameters for the experiment, of the flow regimes and how they determine the corresponding flow behaviours. Dimensionless numbers constructed by combining several physical quantities prove to be highly useful in fluid dynamics experiments (Batchelor (2000)), as influences by peculiar conditions of individual experiments can be eliminated by nondimensionalisation. Empirical experience in the study of rotating fluids (Hide (1969), Hide & Mason (1975)) indicates that two parameters are especially important in shaping the observed flow patterns—that is, thermal Rossby number $\mathcal{R}o$ and Taylor number $\mathcal{T}a$:

$$\mathcal{R}o = \frac{g\alpha\Delta T\Delta D}{\Omega^2 L^2}, \quad (1.1)$$

$$\mathcal{T}a = \frac{4\Omega^2 L^5}{\nu^2 D}. \quad (1.2)$$

Here $\mathcal{T}a$ represents the effect of molecular viscosity, and $\mathcal{R}o$ represents the relative importance of rotation. Ω is the rotation rate, ν the viscosity of the fluid, L the width of the annulus, D the depth of fluid, ΔT the applied

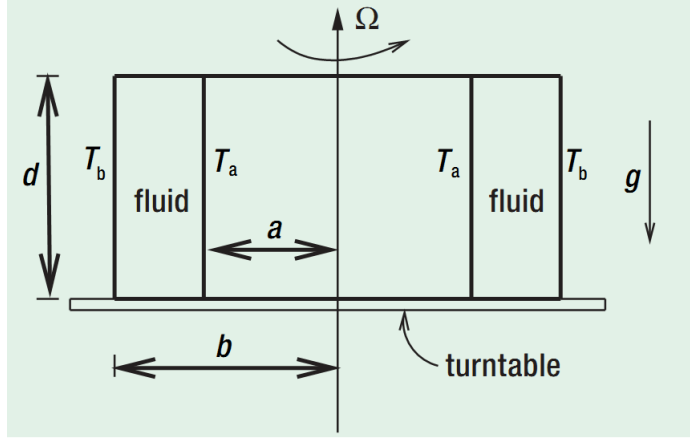


Figure 1.1: A schematic view of the rotating annulus (White (2010)). The working fluid is filled between the inner and outer cylinder, which has radius of a and b respectively. The fluid is forced with the horizontal temperature difference of $T_a - T_b$. Depth of fluid is d .

horizontal temperature difference, α the volumetric expansion coefficient, and g the gravity.

The Taylor number $\mathcal{T}a$ can be rewritten in terms of viscous timescale L^2/ν as:

$$\mathcal{T}a \simeq 4\Omega^2 \tau_\nu^2. \quad (1.3)$$

Using these two parameters, a 2-D parameter space can be constructed with $\mathcal{T}a$ as abscissa and $\mathcal{R}o$ as ordinate. Individual experiments can be located in this parameter space by calculating their values of $\mathcal{R}o$ and $\mathcal{T}a$. Clear trends of regime transition can be revealed by exploring the flow patterns at various locations within the parameter space. The diagram showing the distribution of different flow regimes is referred to as *regime diagram* (see Figure 1.2). At least three distinct categories of regime could be found in such a regime diagram obtained through rotating annulus experiment: axisymmetric steady flow; steady or vacillating regular waves; irregular or turbulent waves.

Baroclinic instability is the primary mechanism for generating waves and eddies, the characteristic length scale of which can be estimated by Rossby deformation radius L_D :

$$L_D = \frac{ND}{2\Omega}, \quad (1.4)$$

where $N = g\alpha\partial T/\partial z$ is the Brunt-Väisälä frequency which is related to the stratification of the fluid. Thus the horizontal scale of baroclinic eddies

tends to be smaller for faster rotating experiments (which have small $\mathcal{R}o$). This can be reflected in Figure 1.2 where smaller $\mathcal{R}o$ corresponds to larger wavenumber.

β -effect could be introduced to the annulus by replacing the bottom plane of the annulus with a sloped boundary which goes higher up from the inner rim to the outer rim with a slope angle δ . This leads to the formation of multiple zonal jets and parallel baroclinic zones at higher rotation rates, which could be explained by Rhines' theory of geostrophic turbulence (see Rhines (1975), Showman et al. (2010)). According to this theory, the latitudinal extent of each baroclinic band can be estimated by the Rhines scale:

$$L_\beta = \pi \left(\frac{U}{\beta} \right)^{1/2}, \quad (1.5)$$

where U is the characteristic horizontal flow velocity, and

$$\beta = \frac{2\Omega \tan \delta}{D}. \quad (1.6)$$

Parametric dependence studies of the rotating annulus are relatively well-established so far. For planetary circulation that occurs within a spherical shell, such parametric dependence has not yet been fully explored. Theoretical development of atmospheric dynamics in the 20th century mainly focused on separate branches or individual components of the global circulation, like mid-latitude fronts and cyclones (see Bjerknes (1919)), planetary waves (Rossby (1939)), instability theories (Charney (1947)) and so on. A grand theory of the general circulation which could quantitatively explain the structure and intensity of the atmosphere in global scale, however, is still under development. Nevertheless, insights of the underlying mechanism of different circulation regimes can be gained by adopting the similar approach in laboratory experiments to the numerical GCM experiments. Our current database of planetary atmospheres is continuously growing thanks to the continuous discovery of extrasolar planets and more observational constraints of the Solar System planets. The regime diagram for planetary circulations established by ensemble numerical experiments could be viewed as a spectrum of possible circulation regimes in which the circulations of rocky (exo)planets can be located and estimated. Atmospheric structure and even climatic conditions on little known rocky exoplanets could also be inferred from such regime diagram, thus lending great relevance to such fundamental studies.

Curiously, most of the GCM studies regarding either Earth or other planets focused more on the very specific conditions of a certain planet

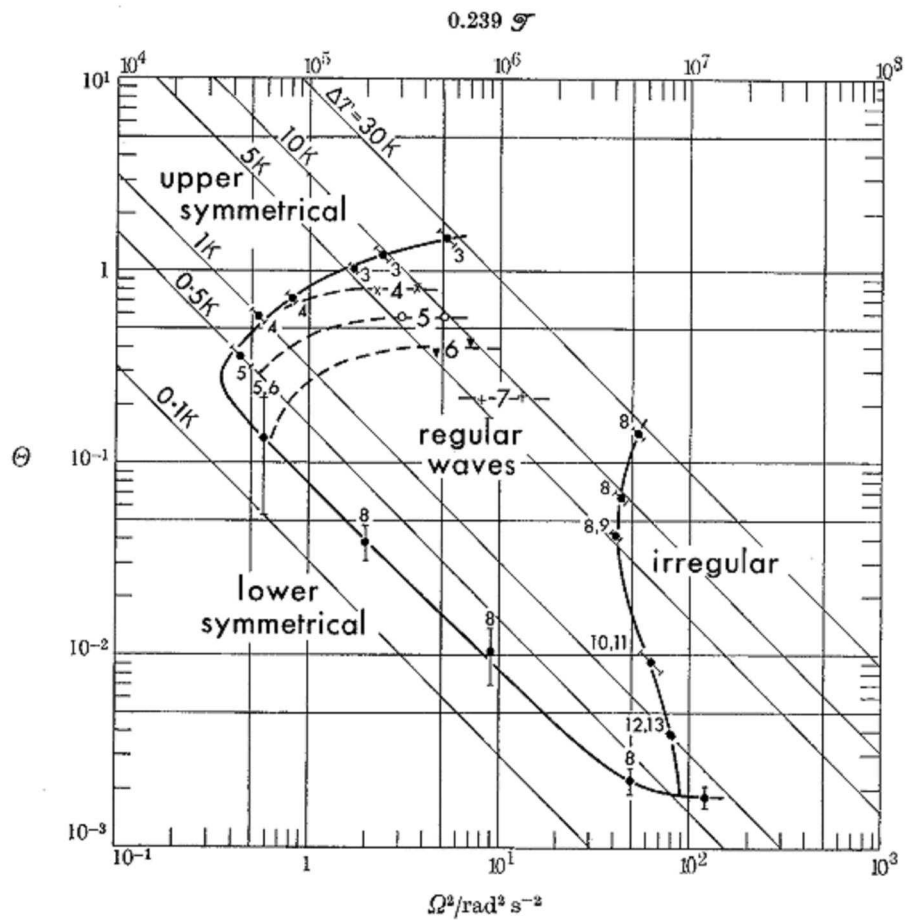


Figure 1.2: Regime diagram from Hide & Mason (1975). Note that for historical reasons, thermal Rossby number is written as Θ rather than $\mathcal{R}o$. 45° slope lines from the top left to the bottom right are experiments with same horizontal temperature difference. Numbers at individual points represent the observed wavenumbers

and the model is usually designed to be as realistic as possible. Sensitivity experiments on parameters like planetary rotation rate, planetary radius and so on has been performed with various aims (see Hunt (1979), Williams & Holloway (1982), Del Genio & Suozzo (1987), Williams (1988a), Williams (1988b)), and Geisler et al. (1983) even came up with a preliminary regime diagram. However, systematic studies of the parametric dependence using idealised numerical models was not paid enough attention. Even in the study of exoplanet atmospheres where observational constraints are scanty, numerical modelling efforts are devoted more to the individual planet rather than to the more generic prototype atmosphere. This constitutes one of the major motivations of my current DPhil project.

1.2 Dimensionless parameters for planetary circulation

Similarity theory is often used to find the characteristic dimensionless parameters in fluid dynamics experiments. For planetary circulation context, Golitsyn (1970) proposed three dimensionless parameters based on this similarity considerations to characterise rocky planetary atmospheric circulations. But his arguments are focused more on the energetics of the planetary atmosphere and based on various assumptions. In this report, we argue that based on the conceptual similarities between the rotating annulus and planetary atmosphere, thermal Rossby number and Taylor number are also the defining dimensionless parameters for planetary circulations. However, modifications need to be made for the transfer from cylindrical to spherical geometry:

$$\mathcal{R}o = \frac{R\Delta\theta_h}{\Omega^2 a^2}, \quad (1.7)$$

where $\Delta\theta_h$ is the equator-to-pole potential temperature difference, a the planetary radius. The planetary counterpart of Taylor number is no longer written in terms of molecular viscosity, since molecular viscosity is not the major dissipation mechanism for large scale atmospheric motions. Instead, a frictional parameter which can be viewed as a substitute of Taylor number can be defined as the following:

$$\mathcal{F}_f = 4\Omega^2\tau_f^2. \quad (1.8)$$

Here τ_f is the characteristic timescale of friction when Rayleigh friction is assumed. Similarly, the radiative forcing can be represented by:

$$\mathcal{F}_r = 4\Omega^2\tau_r^2, \quad (1.9)$$

where τ_r is the radiative time scale defined when Newtonian cooling is assumed. If more realistic radiative transfer scheme other than Newtonian cooling is used to calculate the diabatic heating processes, then there will be more defining dimensionless parameters to be incorporated in the parameter space.

It should be particularly noted that the potential temperature difference $\Delta\theta_h$ appeared in \mathcal{Ro} is not the controllable condition that could be externally set by the experimenter. Instead, it depends on the heat transport efficiency of the atmosphere which is not known directly from the external observable constraints. Therefore, \mathcal{Ro} defined for planetary circulation is a kind of *internal* parameter, in contrast with the \mathcal{Ro} defined for rotating annulus which is an *external* parameter. Ideally, we expect the ultimate parameter space to be constructed by external parameters. Therefore, the $\Delta\theta_h$ should be estimated (parametrised) by some relevant external quantities like stellar irradiance, planetary rotation, radiative properties of atmosphere, etc.

A simple but crude estimation is to replace $\Delta\theta_h$ with the radiative-convective equilibrium temperature difference $\Delta\theta_{he}$. A more reasonable step forward is to introduce a constant diffusion coefficient to represent the effect of dynamic heat transport as the following (Held (1999)):

$$\Delta\theta_h = \frac{\Delta\theta_{he}}{1 + 6\frac{cD}{Ba^2}}, \quad (1.10)$$

where c is the heat capacity of the atmosphere per unit area, D is the constant diffusion coefficient, B the change rate of atmospheric temperature with outgoing thermal radiation (assuming thermal radiation is linear with temperature), and a the planetary radius. According to the arguments of Held (1999), the meridional temperature gradient is significant at extratropical regions where heat transport is mainly assumed by eddies. Overturning Hadley cell is usually efficient enough to even out the temperature inhomogeneity at tropical region. The diffusion coefficient D again could be parametrised by external parameters. A series of parameterisation schemes of eddy diffusivity D have been proposed based on various assumptions of baroclinic eddy activities (Stone (1972), Green (1970), Held & Larichev (1996), and Barry et al. (2002)) as shown in Table 1.1.

Finding out a physically reasonable parameterisation to make the thermal Rossby number \mathcal{Ro} an external parameter is necessary for the ultimate parameter space. A prerequisite for such investigation would be a relatively realistic radiation scheme to describe the diabatic heatings more appropriately than the Newtonian cooling scheme which is a bit *ad hoc*. The con-

Scheme	D
Stone (1972)	$\frac{H^2 N g}{f^2 \theta_0} \frac{\partial \bar{\theta}}{\partial y}$
Green (1970)	$L_{zone}^2 \frac{g}{N \theta_0} \frac{\partial \theta}{\partial y}$
Held & Larichev (1996)	$\frac{g^3}{N^3 \beta^2 \theta_0^3} \left(\frac{\partial \theta}{\partial y} \right)^3$
Barry et al. (2002)	$\left(\frac{e a \dot{q}_{net}}{\theta_0} \frac{\partial \theta}{\partial y} \right)^{3/5} \left(\frac{2}{\beta} \right)^{4/5}$

Table 1.1: Baroclinic eddy diffusivity parametrisation schemes, after Showman et al. (2010). H is the atmospheric scale height, N the buoyancy oscillation frequency, g the gravitational acceleration, f the Coriolis parameter, θ_0 the reference potential temperature, $\partial \bar{\theta} / \partial y$ the R-C equilibrium meridional θ gradient, L_{zones} the latitudinal range of the baroclinic zone, e a constant of order unity, a the planetary radius, \dot{q}_{net} the net radiative heating/cooling per unit mass that the eddy fluxes are balancing.

struction of such a realistic yet generic radiation scheme is the major work of my second year.

1.3 Chapter introductions

In this report, we first present a brief summary of 1st year’s work and an overview of the 2nd year’s work in Chapter 2. This is followed by the description of the 1-D R-C model that was constructed in my 2nd year. The validation of the model is presented in Chapter 4. Chapter 5 shows the work to extend the 1-D model to represent latitudinal variations. Some preliminary explorations of the parametric dependence of atmospheric thermal structure on radiative parameters are discussed in Chapter 6. A summary of the major conclusions and plans for the future work are discussed in Chapter 7.

Chapter 2

First Year Summary and Overview of Second Year

For consistency, a brief summary of my first year's work is presented before we start the main content of the second year's work. First year's work mainly focused on the dynamical respects of the general circulation's dependence on planetary rotation rate (thus the thermal Rossby number \mathcal{Ro}). Major results and conclusions will be recapped here. In the second part of this chapter we present the overview and justifications of the second year's work on 1-D R-C model.

2.1 Summary of first year's work

Numerical experiments using the GCM PUMA* on the parametric dependence of terrestrial circulation regimes on planetary rotation rate were conducted in my first year. The rotation rate ranges from $8\Omega_E$ to $1/16\Omega_E$ (where Ω_E is the Earth's current rotation rate) in our experiments. Values of the characteristic dimensionless parameters for planetary circulation are listed in Table 2.1 as the following.

Here N_J stands for the number of jet streams expected to exist, and is formulated as:

$$N_J = \frac{a}{L_R} = \frac{2}{\pi\sqrt{\mathcal{Ro}}}, \quad (2.1)$$

*PUMA (Portable University Model of Atmosphere) is a spectral GCM using simplified linear physical processes. Newtonian cooling scheme is employed to calculate all diabatic heating/cooling. And the frictional dissipation process in the planetary boundary layer is represented by the Rayleigh friction.

Ω/Ω_E	$\mathcal{R}o$	N_J	F_f
1/16	20.25	0.14	0.62
1/8	5.06	0.28	2.48
1/4	1.27	0.57	9.92
1/2	0.32	1.13	39.67
1	0.079	2.26	158.69
2	0.020	4.53	634.75
4	0.005	9.06	2.54×10^3
8	0.001	18.08	1.02×10^5

Table 2.1: Characteristic Dimensionless numbers of the $1/16\Omega$ to 8Ω experiments

where a is the radius of the planet, L_R the Rhines scale, and $\mathcal{R}o$ the thermal Rossby number. a can be viewed as the characteristic length scale of the planetary domain, while L_R can be viewed as the characteristic meridional scale of the β plane baroclinic eddies.

Clear trends could be seen from Table 2.1 that there tends to be more jet streams as the rotation rate goes higher. This is qualitatively similar to what we observed in the Solar System’s rapid rotators like Jupiter and Saturn, albeit they are gas giants whose governing dynamics of atmospheric circulation is somewhat different from that of the rocky planetary atmospheres. For the terrestrial case ($\Omega/\Omega_E = 1$), the number of jet streams is between 2 and 3, indicating that the Earth is actually a bit beyond the regime where only one jet stream can exist in each hemisphere. These estimates are in reasonable agreement with those produced by Read (2011) based on the experiments of Williams (1988a).

This phenomenon of multiple-jet formation as rotation rate goes higher predicted by Rhines’ theory can be illustrated in Figure 2.1, which shows the zonal mean cross-sections of zonal wind and meridional mass streamfunction from 8Ω to $1/16\Omega$. Another trend shown in this figure is that as the rotation rate slows down, Hadley cells expand in the latitudinal direction and get stronger, pushing the subtropical jets poleward. This is qualitatively similar to the atmosphere of slowly rotating planets like Venus and Titan, where the global circulation is featured by dominating Hadley cells.

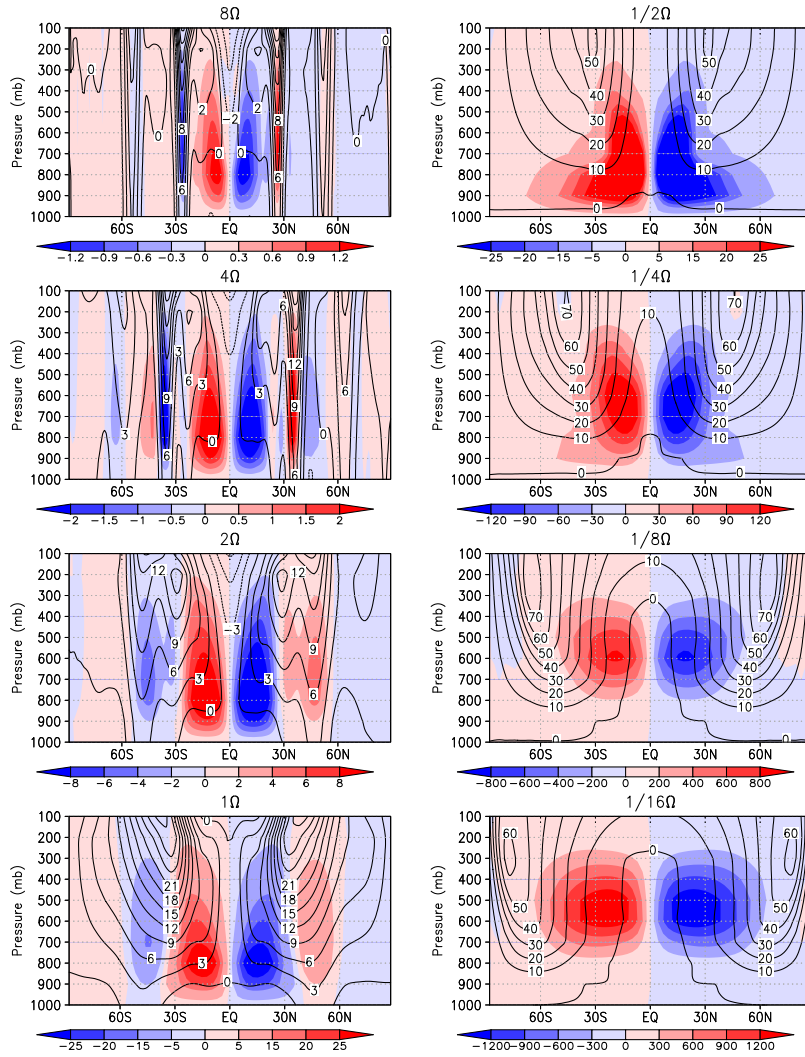


Figure 2.1: Zonal mean zonal wind and the meridional mass streamfunction. Contours are zonal winds in m/s , and shades are the meridional mass streamfunction in $10^9 kg/s$.

2.2 Second year’s work—overview and justification

2.2.1 Overview

The major work of my second year is the construction and validation of a semi-grey radiative-convective (R-C) scheme. It is built in a 1-D column form as a first step towards being fully coupled with the 3-D GCM. Such a 1-D model assumes that the electromagnetic spectrum of the radiation transferred in atmosphere can be divided into two bands: the short-wave band representing the high-energy radiation from the parent star, and the long-wave band representing the thermal radiation from the atmosphere and the planetary surface. In each band, the extinction coefficient is assumed to be constant with respect to the pressure and the wavelength, thus named *semi-grey*. The radiatively active absorbers in the atmosphere are assumed to distribute uniformly (constant mass concentration for example) across the vertical direction. A simple convective adjustment scheme following the treatment of Manabe & Wetherald (1967) is incorporated in this model to prevent the radiative heating/cooling from producing a statically unstable vertical temperature profile. A programme calculating the incoming stellar radiation at top of atmosphere is developed and coupled with the 1-D model to represent the latitudinal variation of the temperature field.

2.2.2 Justification

The reason of constructing such a semi-grey R-C model is to make a step forward to the reasonable estimation of the meridional temperature difference by external parameters. As stated in Chapter 1, the radiative-convective equilibrium temperature difference $\Delta\theta_{he}$ could be viewed as a crude approximation of $\Delta\theta_h$, although other more complex parametrisations in terms of eddy diffusivity are perhaps more accurate if given appropriate values of diffusivity. Nevertheless, this gives a practical start point from which more advanced investigations could be derived.

We made the assumption of semi-grey atmosphere so that the results could be as generic as possible. More complex radiative schemes would tend to include the absorption lines of specific gas constituents, the radiative properties of various aerosols, as well as the inhomogeneous spatial distribution of absorbers. Although the inclusion of such realistic processes could possibly generate more accurate thermal structures than our dual-band semi-grey model, we maintain that generalisable results could only be yielded from

models with relatively simple and clear representation of physical processes. In particular, for the study of climate conditions on exoplanets where little data is available, such approach of dual-band radiative transfer scheme is especially useful for gaining insights about the possible atmospheric thermal structure (see the recent work of Heng et al. (2011)).

Computational efficiency, in addition, is a major advantage of using such a simplified R-C model. For the terrestrial setting of parameters, the model reaches the R-C equilibrium state within 10 minutes of integration (starting from an isothermal atmosphere of 280 K at all layers), which is far efficient than the more complicated multi-band or line-by-line schemes. This practical consideration of computational speed is especially important for this project since large ensemble runs of numerical models are required to explore the parameter space relatively thoroughly (see the discussions in Chapter 7).

It should be noted that the assumption of dividing the radiative spectrum into two bands (long-wave and short-wave) might not always be realistic at first sight, especially for those close-in exoplanets (hot jupiters, for example) in which case the planet lies extremely close to the parent star and the atmosphere could be heated up to thousands of Kelvins, which is comparable to the effective temperature of the star. The distinguish of wavelength between stellar radiation and the planetary radiation would be very small for such cases, thus making the division in this context less meaningful. Nevertheless, we argue that this special scenario could be modelled under current assumptions by giving roughly same optical properties to the two bands, which would essentially reduce the two bands scheme to one band, therefore including the close-in exoplanet atmospheres as a subset within the parameter space we will explore.

The major potential weakness of using this simplified scheme is that the influence of local concentration of absorbers in the vertical direction (like the UV-absorbing ozone layer of the Earth's atmosphere) may not be accurately reflected in our model. But in principle, this does not affect the estimation of surface temperature and general thermal structure of the atmosphere emulated by our model (see the discussions in Chapter 4). Our model is by no means intended to do very accurate simulations of any specific planet's atmosphere. Instead, it should be viewed as a heuristic model which could estimate the general and fundamental attributes of the atmospheric vertical thermal structure that are common to many rocky planets. In this sense, it resembles the conceptual model by Taylor (2010) which regards the vertical structure of the atmosphere to consist of an isothermal stratosphere and a troposphere with constant dry adiabatic lapse rate. In fact, radiation

schemes with similar complexity like ours have been proposed by theoreticians through modifying various conditions and assumptions of the classical grey atmosphere (see the analytical attempts by Weaver & Ramanathan (1995)), and a series of highly inspirational implications have been deduced analytically which are more powerful and applicable than classical grey atmosphere in helping the study of planetary atmospheres. This again justifies our current exploration using such kind of simplified numerical schemes.

Chapter 3

1-D Radiative-Convective Model

In this chapter, we will focus on the construction of the semi-grey radiative-convective scheme. As a preliminary step, the scheme is implemented in a 1-D column fashion. Section 3.1 describes how the model represents radiative transfer processes in a dual-band form. Section 3.2 presents the mechanism of the convective adjustment scheme used in our model. Section 3.3 shows the configuration of the model's vertical discretisation.

3.1 Radiative transfer

The process of radiative transfer in the atmosphere is highly complex and always poses a significant challenge to numerical modellers. Different gases in the atmosphere have different absorption and scattering characteristics, at different wavelengths. Line-by-line calculations could provide the most accurate representation of the radiative effect of each gaseous composition in the atmosphere, but is computationally very demanding. Most GCMs take a more practical approach of grouping the individual absorption lines into several bands which saves a lot of computer resource. In our 1-D radiative-convective model, we adopt the similar philosophy and construct a highly simplified scheme of only two bands: the long-wave thermal radiation band ($1.7\sim 250\ \mu m$) and the short-wave stellar radiation band ($0.1\sim 5.0\ \mu m$). Furthermore, we assume that in each band, the extinction coefficient is constant with respect to the wavelength (i.e. the atmosphere is grey in each band). Scattering effects are only partially reflected in the constant extinction coefficient. For the simplicity we assume that there is no condensable con-

stituents in the atmosphere, hence no cloud coverage. Radiatively active gases or aerosol absorbers are assumed to be well-mixed in the vertical direction.

The model has only one dimension which represents the vertical direction. Thus the result produced by this model should be viewed as a globally averaged climate state with no horizontal or temporal variations. Radiative transfer processes are modelled with the assumption of plane parallel atmosphere, which regards the atmosphere to be a flat disk in which there are only upward and downward beams of radiation. The diffuse approximation (see Andrews (2010)) is employed to keep the radiative transfer equation in its classical form:

$$-\frac{dF^\uparrow}{d\tau^*} + F^\uparrow = \pi B(T), \quad (3.1a)$$

$$\frac{dF^\downarrow}{d\tau^*} + F^\downarrow = \pi B(T). \quad (3.1b)$$

Here τ^* is the scaled optical depth. In our scheme, it is estimated by (Ramanathan et al. (1985)):

$$\tau^* = \left(1.5 + \frac{0.5}{1 + 4\tau + 10\tau^2}\right)\tau, \quad (3.2)$$

in which $\left(1.5 + \frac{0.5}{1 + 4\tau + 10\tau^2}\right)$ is known as the diffusivity factor representing the effect of integrating over various directions within a hemisphere (which seems straightforward at first sight to integrate, but could be fairly tricky in practice), and τ is the optical depth measured *vertically* from top of the atmosphere. Some radiative transfer schemes use a constant value of diffusivity factor, like 1.5 (Goody & Yung (1989)) or 1.66 (Andrews (2010)) for example, to approximate the integration. Our approach here is more accurate than the constant-value approximation (see the discussions of Ramanathan et al. (1985)).

Figure 3.1 illustrates the radiative transfer processes represented by the 1-D model. There are 40 vertical layers in the standard setting. Each layer has an upper boundary and a lower boundary, which are referred to as levels. Thus 40 layers indicates 41 levels in the vertical direction, with level 1 representing TOA, and level 41 representing the ground. Stellar radiation goes downward from the top of atmosphere and gets partially extinguished on its way to the ground. When it reaches the planetary surface, part of it is absorbed by the ground and the other part reflected back towards the space. The default value of planetary bond albedo is assumed to be 0.3 which is the globally averaged albedo of the Earth. On the other hand, the planetary

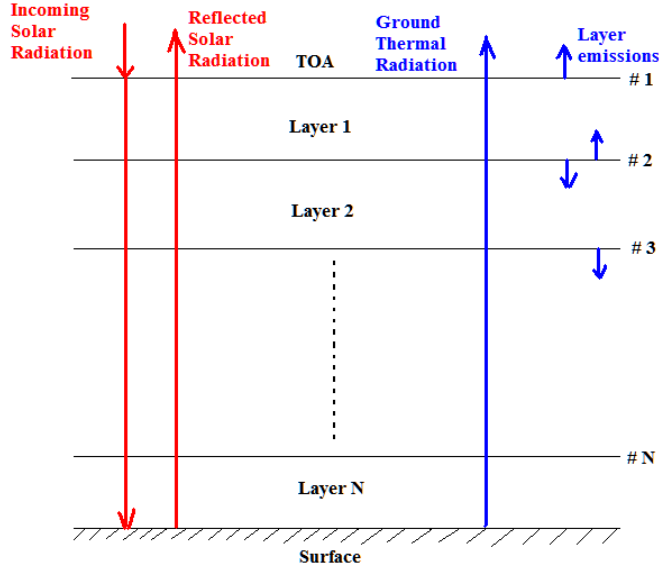


Figure 3.1: Schematic of the radiative transfers in the 1-D model, levels are marked by #.

surface as well as the atmosphere itself is emitting long wave thermal radiation. The model starts from an isothermal atmosphere. Radiative fluxes (measured in Wm^{-2}) are calculated at levels, and heating rates are then calculated at layers based on the net fluxes of adjacent levels. Temperatures are updated by the calculated heating rates at each layer. This temperature profile is then further updated by a convective adjustment scheme. When the temperature difference at consecutive timesteps becomes lower than a certain threshold value (which is usually set to $10^{-3} K$ or even smaller), the atmosphere is assumed to be in a radiative equilibrium state.

The optical thickness of an arbitrary layer n for a radiation beam with zenith angle θ_z is defined by:

$$\tau(n, \mu) = \frac{1}{\mu} \int_b^t k \rho_e dz \quad (3.3)$$

in which $\mu = \cos \theta_z$, $k = k_a + k_s$ is the extinction coefficient which is the sum of absorption coefficient and scattering coefficient (Andrews (2010)), b and t stands for the bottom and top of the layer, and ρ_e is the density of the gas composition that attenuates the radiation. Using the hydrostatic

relationship, the equation can be rewritten as :

$$\tau(n, \mu) = \frac{k \rho_e \Delta p}{\mu \rho_a g}, \quad (3.4)$$

where ρ_a is the density of the environment atmosphere, Δp the pressure difference between the top and bottom of layer n , and g the constant gravitational acceleration.

If we define $k^* = k\rho_e/\rho_a$ as the scaled extinction coefficient, then $\tau(n, \mu)$ can be expressed in a more compact form:

$$\tau(n, \mu) = \frac{k^* \Delta p}{\mu g}. \quad (3.5)$$

This is the expression used in our algorithm to calculate the optical thickness of layer n .

For the short-wave stellar radiation, its magnitude is attenuated exponentially during its transfer within the model atmosphere. For example, the downward stellar radiation flux at level n is:

$$F^\downarrow(n, \mu) = F^\downarrow(n-1, \mu)e^{-\tau(n, \mu)}, \quad (3.6)$$

with the upper boundary condition:

$$F^\downarrow(1, \mu) = S_0\mu \quad (3.7)$$

in which S_0 is the solar constant.

At the ground level, this downward stellar radiation flux is partly absorbed according to the prescribed planetary albedo and the others get reflected back upwards, which is also subject to this exponential extinction.

Similarly, the downward long-wave thermal radiation flux at level n can be calculated by the following equation:

$$F^\downarrow(n) = E^\downarrow(n) + F^\downarrow(n-1)e^{-\tau(n)/D}, \quad (3.8)$$

where $D = \frac{1}{1.5 + \frac{0.5}{1+4\tau+10\tau^2}}$ is the reciprocal of the diffusivity factor, and could be viewed as μ averaged over different directions. $E^\downarrow(n)$ is the downward atmospheric thermal emission of layer n , which is estimated by (see Lacis & Oinas (1991)):

$$E^\downarrow(n) = (B(T_b) - B(T_t)e^{-\tau(n)/D}) \frac{\tau(n)}{\tau(n) - D \lg [B(T_t)/B(T_b)]}. \quad (3.9)$$

Here $B(T_b)$ is the blackbody radiation flux at bottom boundary of layer n , and $B(T_t)$ is the blackbody radiation flux at the top boundary.

For the upward long-wave thermal radiation, we have

$$F^\uparrow(n) = E^\uparrow(n) + F^\uparrow(n+1)e^{-\tau(n)/D}, \quad (3.10)$$

in which $E^\uparrow(n)$ is the upward atmospheric thermal emission of layer n estimated by:

$$E^\uparrow(n) = (B(T_t) - B(T_b)e^{-\tau(n)/D}) \frac{\tau(n)}{\tau(n) - D \lg[B(T_b)/B(T_t)]}. \quad (3.11)$$

Using these equations, we can calculate the net radiative flux at each model level, and hence deduce the heating rate of an arbitrary layer n as:

$$Q(n) = \frac{g}{c_p} \frac{F_n(n+1) - F_n(n)}{p(n+1) - p(n)}, \quad (3.12)$$

in which g is the gravitational acceleration, c_p the specific heat capacity at constant pressure of the atmosphere, $F_n(n+1)$, $F_n(n)$ and $p(n+1)$, $p(n)$ refer to the net radiative fluxes and pressures at level $n+1$ and level n respectively.

It should be noted that when calculating short-wave radiation (see Equation 3.6), fluxes and heating rates are calculated with a specific value of stellar zenith angle θ_z , which would vary with geographical location and time in a year. In order to account for the globally averaged annual mean state, we need to perform the following integration to the short-wave stellar radiation heating rate (Crisp (1989)):

$$\left. \frac{dT}{dt}(n) \right|_{GA} = \frac{1}{2} \int_0^{\pi/2} \frac{dT}{dt}(\theta_z, n) \sin(\theta_z) d\theta_z, \quad (3.13)$$

in which the subscript GA stands for global average. An 8-point Gaussian quadrature algorithm is used to estimate this integral.

Temperature changes at layer n caused by radiative heating/cooling are calculated by:

$$T(n) = T_0(n) + Q(n)\Delta t, \quad (3.14)$$

where $T_0(n)$ is the temperature of layer n at the previous time step, $Q(n)$ the total heating rate (sum of long-wave and short-wave heating), Δt the length of one time step ($\Delta t = 1$ hour in the standard setting).

In particular, the ground is assumed to be a black body in radiative equilibrium. Thus the following relationship stands:

$$F_{ns}(N+1) + F_l^\downarrow(N+1) = \sigma T_g^4, \quad (3.15)$$

in which $F_{ns}(N+1)$ refers to the net short-wave stellar radiation flux at level $N+1$ (planetary surface level), $F_l^\downarrow(N+1)$ the downward longwave thermal radiation flux at ground level, σ the Stefan-Boltzmann constant, and T_g the ground temperature.

3.2 Convective adjustment

The radiative equilibrium temperature profile, given by the pure radiative transfer scheme, has a significant temperature discontinuity near the ground level and is statically unstable to vertical perturbations. Convection could easily be triggered in an atmosphere with such a lapse rate, transporting heat upwards and eventually modifying the temperature profile. First introduced by climate modellers in the 1960s (Manabe & Strickler (1964), Manabe & Wetherald (1967)), convection scheme nowadays has grown to a formidable complexity with cloud-resolving capability (see Emanuel (1994), McGuffie & Henderson-Sellers (2005)). In our model, we implement the simple dry convective adjustment scheme proposed by Manabe & Strickler (1964), which is not a realistic scheme that explicitly resolves the vertical overturning of convections, but rather a numerical re-evaluation of the temperature profile that is applied when the lapse rate exceeds a prescribed critical value.

The convective adjustment subroutine in our model is run everytime the temperature profile has been updated by the radiative heating. It scans upwards from the ground level to check whether the temperature difference between each two adjacent layers exceeds the temperature difference required by the critical lapse rate, which is set to be the dry adiabatic lapse rate ($\Gamma = g/c_p$). If yes, the temperatures of these two layers will be modified with the constraint of conserving total enthalpy (i.e. total potential energy), and the local lapse rate will be restored to the critical value. For the bottom layer (layer N) adjacent to the ground, the temperatures of the atmosphere and the ground are modified according to:

$$\frac{c_p}{g} \Delta p_N [T_N^{(1)} - T_N^{(0)}] = \sigma \Delta t \{ [T_g^{(0)}]^4 - [T_g^{(1)}]^4 \}, \quad (3.16a)$$

$$T_N^{(1)} = T_g^{(1)} - LRC_N, \quad (3.16b)$$

in which Δp_N is the pressure difference between level N and level $N+1$, $T_N^{(1)}$ the temperature of layer N after the adjustment, $T_N^{(0)}$ the temperature of layer N before the adjustment, $T_g^{(0)}$ the temperature of the ground before the adjustment, $T_g^{(1)}$ the temperature of the ground after the adjustment, and

LRC_N is the critical temperature difference between the atmosphere and the ground. The first equation basically states that the enthalpy gain of the bottom layer atmosphere equals to the enthalpy lost of the ground. The second equation represents the constraint that critical lapse rate is restored after the adjustment.

For layers (e.g. n and $n + 1$) not in direct contact with the ground, modification is done with the following constraint:

$$\frac{c_p}{g} \left\{ \Delta p_n [T_n^{(1)} - T_n^{(0)}] + \Delta p_{n-1} [T_{n-1}^{(1)} - T_{n-1}^{(0)}] \right\} = 0, \quad (3.17a)$$

$$T_n^{(1)} - T_{n-1}^{(1)} = LRC_n. \quad (3.17b)$$

After this modification, the temperature profile is scanned again to check whether it is statically stable. If not, the above procedures will be repeated until a stable profile is reached.

3.3 Vertical discretisation

The σ -coordinate is used in the vertical direction of the R-C model. It is defined on model levels as (Manabe & Strickler (1964)) :

$$\sigma(n) = f(n)^2(3 - 2f(n)) \quad (3.18)$$

in which

$$f(n) = (n - 0.5)/N, \quad (3.19)$$

and $n = 1, 2, 3, \dots, N$, N is the total number of layers.

Pressure of level n is then

$$p(n) = \sigma(n)p_s, \quad (3.20)$$

where $p_s = 101325 \text{ Pa}^*$ is the constant surface pressure of the model atmosphere, and $p(N + 1) = p_s$.

This vertical discretisation scheme leads to an atmospheric layering that has high resolution near both the top and the bottom of the atmosphere.

Note that parameters like p_s , k_{iw}^ , k_{sw}^* , c_p , g , S_0 and so on can be varied in our 1-D model. The default setting is the Earth's values as we see in this chapter. But that does not mean that these parameters are fixed numbers.

Chapter 4

Model Validation

The R-C model constructed using principles stated in the previous chapter needs to be validated before using it to investigate the parameter space or coupling it to the 3-D GCM. In this chapter, we will present several validation experiments of this 1-D R-C model. Section 4.1 presents the validation against the analytically solvable thermal structures of a grey atmosphere. Section 4.2 shows the model's capability at modelling terrestrial temperature field. Section 4.3 further shows the encouraging results gained when the corresponding parameters are tuned to values for Mars, which fit well with the observations.

4.1 Grey atmosphere validation

The grey atmosphere, as defined in various textbooks (Andrews (2010), Houghton (2002)), refers to an atmosphere that is transparent to the incoming stellar radiation but opaque to the planetary thermal radiation, with a constant extinction coefficient for the thermal radiation*. By further adopting the diffuse approximation in the thermal radiation band, we can use two-stream calculations to analytically derive the expression of upward and downward radiative fluxes at each level as the following(Andrews (2010)):

$$F^\uparrow = \frac{1}{2}F_0(2 + \tau^*), \quad (4.1a)$$

*Perhaps it is more appropriate to call this type of atmosphere semi-grey, as the extinction coefficient is constant only for the long-wave band, rather than for all wavelengths. However, we will follow the meteorological convention to call it a grey atmosphere, and use semi-grey to refer to the dual-band atmosphere described in Chapter 3.

$$F^\downarrow = \frac{1}{2}F_0\tau^*, \quad (4.1b)$$

and the thermal emission at scaled optical depth τ^* is

$$\pi B(T) = \sigma T^4 = \frac{1}{2}F_0(1 + \tau^*), \quad (4.2)$$

where F_0 is the incoming stellar flux at the top of atmosphere.

For the ground level τ_g^* , thermal emission of the ground (which is assumed to be a blackbody with temperature T_g) must equal the upward long-wave flux at this level:

$$\sigma T_g^4 = F_0(1 + \frac{1}{2}\tau_g^*) \quad (4.3)$$

In the 1-D R-C model, we assume that the scaled extinction coefficient k^* is constant with respect to height. If we use the same assumption here to this analytical model, we can then obtain the following relationship:

$$F^\uparrow(z) = \frac{1}{2}F_0\left(2 + \tau_g^*e^{-z/H_a}\right), \quad (4.4)$$

$$F^\downarrow(z) = \frac{1}{2}F_0\tau_g^*e^{-z/H_a}, \quad (4.5)$$

$$T(z) = \left[\frac{F_0}{2\sigma}(1 + \tau_g^*e^{-z/H_a})\right]^{1/4}, \quad (4.6)$$

where H_a is the pressure scale height of the atmosphere.

Figure 4.1 shows the vertical profiles of $F^\uparrow(z)$, $F^\downarrow(z)$, and $T(z)$ predicted by the radiative transfer theories using corresponding values for the Earth. For Earth's atmosphere, the total scaled optical depth $\tau_g^* = 2.0$ (see Andrews (2010)), and the annually and globally averaged incoming stellar radiation at the top of atmosphere $F_0 = 240 \text{ Wm}^{-2}$. In the right panel, $T_{strat} = 215\text{K}$ is the stratospheric temperature, $T_b = 282\text{K}$ is the temperature of the bottom layer atmosphere, and $T_g = 303\text{K}$ is the surface temperature of the ground.

Figure 4.2 shows the corresponding upward and downward fluxes calculated by the 1-D numerical model. The model is executed with convective adjustment switched off, and the short-wave extinction coefficient is set to zero. The long-wave scaled extinction coefficient is set to $k_{lw}^* = 0.001 \text{ cm}^2\text{g}^{-1}$ so that the long-wave scaled optical depth at the ground level is $\tau_g^* \approx 2.0$, which is approximately the terrestrial value. The upward long-wave flux in this plot is 240 Wm^{-2} which balances the incoming short-wave stellar radiation. At the ground level, the values of upward and downward fluxes

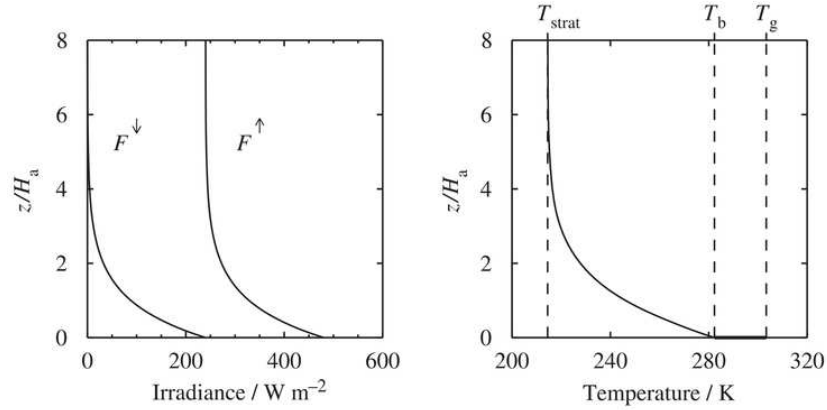


Figure 4.1: Analytically calculated upward and downward long-wave radiative fluxes (left) as well as the radiative equilibrium temperature profile (right), plotted against z/H_a . See Andrews (2010)

are $479 W m^{-2}$ and $240 W m^{-2}$ respectively, which fit well with the values in Figure 4.1. Figure 4.3 shows the radiative equilibrium temperature profile produced by the 1-D model. The stratospheric temperature, bottom layer temperature and the surface temperature all approximately agree with their counterparts in Figure 4.1.

By comparing the radiative fluxes as well as the temperature profile produced by the 1-D model with the analytical results for Earth’s atmosphere, we can conclude that the radiative transfer processes are correctly represented with an accuracy to a satisfactory extent.

4.2 Modelling Earth’s atmosphere

As we can see in the previous section, there is a temperature discontinuity at ground level in a classical grey atmosphere. Such an abrupt change of temperature at a single vertical level implies that the atmosphere is statically unstable near the ground, and convective activity will easily be triggered to decrease this temperature lapse rate. Besides, in Earth’s atmosphere, short-wave extinction by various gaseous constituents (particularly ozone) is not negligible. In this section, we will switch convective adjustment and short-wave extinction on to see how well the 1-D model could represent the vertical temperature profile of the Earth. The scaled extinction coefficient for short-wave stellar radiation is set to $k_{sw}^* = 0.00019 cm^2 g^{-1}$ to produce a reasonable estimation of the solar radiation flux absorbed by surface ($168 W m^{-2}$) that

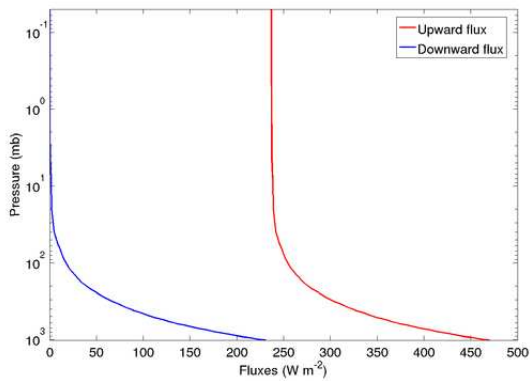


Figure 4.2: Upward and downward long-wave radiative fluxes calculated by the 1-D model with $\tau_g^* \approx 2.0$, and $F_0 = 240 \text{ W m}^{-2}$. Vertical axis is pressure in log scale, which is proportional to z/H_a as used in Figure 4.1.

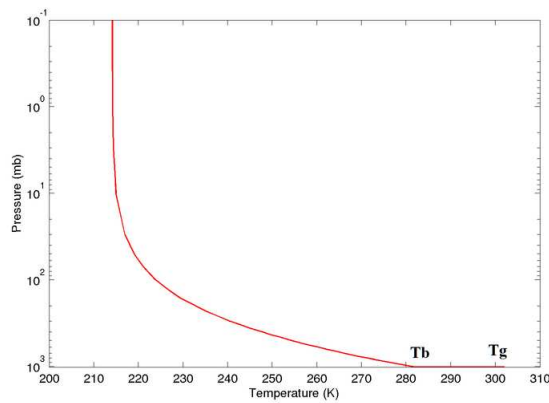


Figure 4.3: Vertical temperature profile calculated by the 1-D model with $\tau_g^* \approx 2.0$, and $F_0 = 240 \text{ W m}^{-2}$. Vertical axis is pressure in log scale, which is proportional to z/H_a as used in Figure 4.1.

fits with the observed climatological value.

Figure 4.4 shows the radiative-convective equilibrium temperature profile compared with the pure radiative equilibrium profile for the classical grey atmosphere. Convective adjustment modifies mainly the temperatures of the lower atmosphere, because the radiative equilibrium profile is only unstable in the lower part. The static stability of a radiative equilibrium temperature profile can be interpreted analytically (see Satoh (2004)) as the following.

Assume that the vertical distribution of the radiatively active constituents in the atmosphere is

$$q = q_0 \left(\frac{p}{p_s} \right)^\alpha, \quad (4.7)$$

in which q is the mass concentration of the constituents at pressure level p , q_0 the value of q at ground level, p_s the surface pressure, and α a constant. If the diffusivity factor for long-wave radiation transfer is assumed to be a constant value of $3/2$, then the stability criterion for the radiative equilibrium profile is

$$\alpha < 4 \frac{R_d}{c_p} - 1, \quad (4.8)$$

where R_d is the gas constant of dry atmosphere, and c_p is the specific heat capacity at constant pressure of the atmosphere (see Satoh (2004) for detailed discussions).

The atmosphere itself is everywhere stable if the above criterion is satisfied. For our numerical simulation, $\alpha = 0$ (which means uniform mass concentration), and $R_d/c_p = 2/7$ for Earth's dry atmosphere made of bi-atomic molecules. The above criterion, therefore, is satisfied for our model atmosphere. The only unstable region is the bottom layer of the atmosphere which is in direct contact with the surface, where there is a significant temperature jump between the warm surface and the cool atmosphere. Convective adjustment, therefore, is only performed to this bottom atmospheric layer. This explains why the two curves in Figure 4.4 are highly overlapped for most of the upper and middle atmospheric region.

The radiative-convective equilibrium temperature profile and the pure radiative equilibrium profile for non-zero short-wave extinction are shown in Figure 4.5. The temperature of the isothermal stratosphere is warmer in this case than that of the classical grey atmosphere, because of the short-wave absorption in the stratosphere. Since the atmosphere absorbs some of the incoming stellar radiation, the radiation eventually absorbed by the ground is decreased, thus leading to a lower and more modest radiative-equilibrium surface temperature of $299K$. This value is further reduced by the convective adjustment to $297K$, still a bit higher than the global average

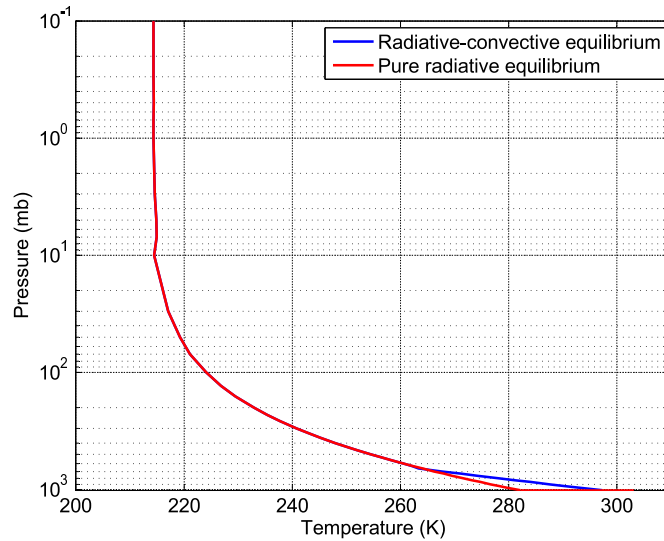


Figure 4.4: Comparison of radiative-convective equilibrium temperature profile and the pure radiative temperature profile for grey atmosphere. Calculated with $\tau_g^* \approx 2.0$, and $F_0 = 240 \text{ Wm}^{-2}$.

of the Earth, which is approximately 288K . But considering the simplicity of this model and the crude assumptions we made (e.g. dual-band semi-grey, dry convective adjustment), the result is reasonably good.

The radiative-convective temperature profile predicted by the 1-D semi-grey model, which features an isothermal stratosphere and a statically stable troposphere, is at first sight quite different from the zigzag temperature profile observed on Earth (see Figure 4.6). The 1-D model assumes that the short-wave absorbers are uniformly distributed in the vertical direction (same mass concentration everywhere), thus there would be no local concentration of absorbers to create a local temperature maximum. On Earth, however, the existence of a considerably concentrated ozone layer at altitudes of $30 - 40 \text{ km}$ creates a temperature maximum at the top of the stratosphere (roughly the 1 mb level in Figure 4.6). If the ozone is not locally concentrated in a certain layer but rather spread uniformly in the vertical direction, there will be no temperature maximum in the blue curve. The zigzag profile will then tend to relax towards the middle value, which could be approximately represented by the red curve in Figure 4.6. On the other hand, if we remove ozone from the atmosphere, there will be no significant absorption of solar radiation, and the vertical temperature structure will tend to resemble the

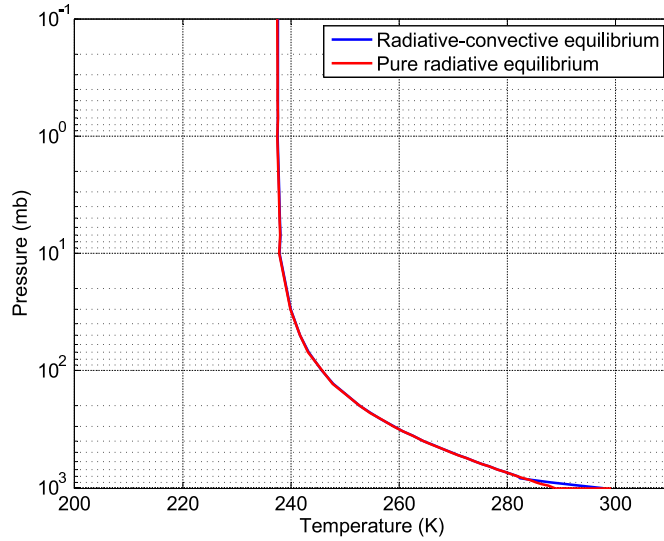


Figure 4.5: Comparison of radiative-convective equilibrium temperature profile and the pure radiative temperature profile for terrestrial atmosphere. Calculated with $k_{sw}^* = 0.00019 \text{ cm}^2\text{g}^{-1}$, $k_{lw}^* = 0.001 \text{ cm}^2\text{g}^{-1}$, and $F_0 = 240 \text{ Wm}^{-2}$.

classical grey atmosphere curve (magenta) in Figure 4.6, which better predicts the troposphere structure and the tropopause temperature. Therefore, apart from features that are related to the distribution of absorbers, the fundamental attributes of the atmospheric thermal structure (e.g. surface temperature, lapse rate, upper atmospheric temperature and so on) could be predicted reasonably well by the model.

4.3 Modelling Martian atmosphere

The Martian atmosphere is largely composed of CO_2 (95.3% by mole fraction), with trace amounts of water vapor and various other gases. Compared with the Earth and Venus, Mars is particularly convenient to study using our 1-D R-C model, mainly because it has no locally concentrated short-wave absorbing gas components like the ozone layer on Earth, nor does it have any dense cloud layers which significantly reshape the temperature profile like what we find on Venus (see Taylor (2010)). The annual mean globally averaged thermal structure, therefore, should be calculated by our 1-D model to a reasonably accurate extent, although the transient yet radiatively signifi-

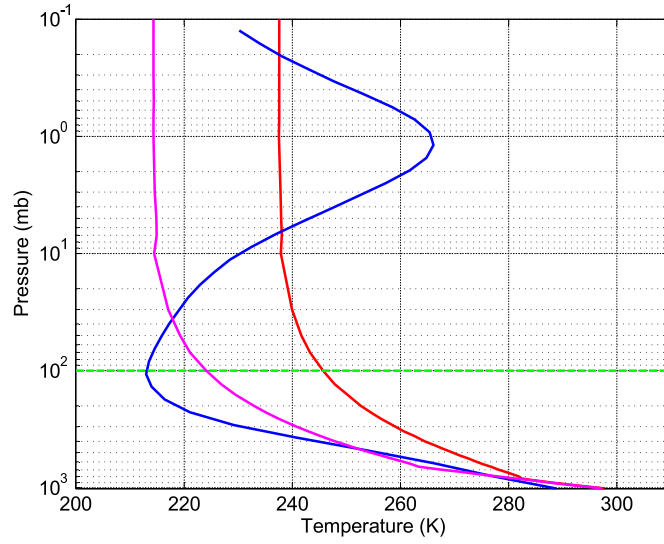


Figure 4.6: Comparison of the observed Earth's temperature profile (blue curve, Fleming et al. (1990)) with R-C equilibrium temperature profile produced by the 1-D model (red) as well as the R-C equilibrium profile of classical grey atmosphere (magenta). Calculated with $k_{sw}^* = 0.00019 \text{ cm}^2 g^{-1}$, $k_{lw}^* = 0.001 \text{ cm}^2 g^{-1}$, and $F_0 = 240 \text{ W m}^{-2}$. Green dash line represents the tropopause of the observed profile.

cant dust storms prevailing on this planet are not represented in the model physics. Plus, it should be noted that, unlike the case of Earth and Venus, the annual mean globally averaged climatic conditions for Mars are somewhat less meaningful due to the stronger seasonal variability caused by the low thermal inertia and the large orbital eccentricity (Taylor (2010), Read & Lewis (2004)). Thus, individual in-situ observations of the vertical thermal structure could differ considerably from the mean climatological structure.

In order to model the Martian atmosphere, we set $p_s = 650 \text{ Pa}$, $c_p = 830 \text{ Jkg}^{-1}\text{K}^{-1}$, $g = 3.74 \text{ ms}^{-2}$ (see Taylor (2010)). Extinction coefficients are set as $k_{lw}^* = 0.05 \text{ cm}^2\text{g}^{-1}$, and $k_{sw}^* = 0$ (assuming dust-free atmosphere). Figure 4.7 shows the observational and model produced vertical temperature profiles of the Martian atmosphere. The upper panel shows the MGS radio occultation observations made near Tharsis at late afternoon and night of $L_s = 150^\circ$. The lower panel is the result of our 1-D model simulation, which should be viewed as annual mean global average. We assume a dust-free atmosphere (i.e. no dust storm or dust lifting) by setting the atmosphere to be transparent at short-wave radiation band, since the optical depth at this band is mainly caused by suspending dust aerosols. Dry convective adjustment is switched off because the convective activities on Mars is not efficient enough to remove the temperature discontinuity near the ground. The calculated profile with such crude settings is surprisingly good compared with the observations. The model simulated profile, if plotted in upper panel, will lie in the middle of the night profiles and late-afternoon profiles, with a near-surface temperature of 225K and 40km level temperature of approximately 177K . It will be reasonable to say that if given an accurate short-wave extinction coefficient caused by dust, the calculated temperature profile could even better emulate the individual observations. But combined with the discussion in the previous two sections, it is clear that our 1-D model is relatively competent at modelling the annual mean globally averaged thermal structures of the rocky planet atmospheres.

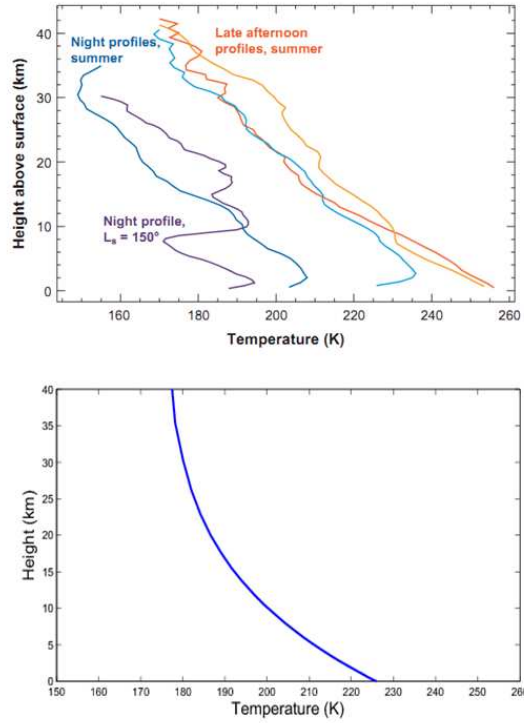


Figure 4.7: Comparison of the observational temperature profile and the model simulated temperature profile of Mars. Upper panel shows MGS radio occultation data. Both Late-afternoon and night time temperatures are shown from mid-latitudes during summer. Observations are made at $L_s = 150^\circ$ (Smith (2008)). Lower panel shows 1-D R-C model results.

Chapter 5

Extended 1-D R-C Model with Latitudinal Variations

The 1-D R-C model described in the last chapter could only predict the global average conditions, whereas the horizontal inhomogeneities, especially latitudinal variations, are not represented. The temperature gradient in the latitudinal direction (north-south) is the major driver of the global circulation. One step further in determining the atmospheric thermal structure is then to reasonably reflect this latitudinal variation. In this chapter, we extend the 1-D R-C model to represent vertical thermal structures at different latitudes. This is done by forcing the 1-D model with the mean stellar radiation as well as the mean stellar zenith angle at different latitudes.

5.1 Incoming stellar radiation (ISR) at top of atmosphere for different latitudes

The instantaneous incoming stellar radiation at the top of the atmosphere for a certain location on a planet depends on a variety of factors: the local time, the latitude, the obliquity of the planet, and the stellar constant at the mean distance between the planet and the star. For a non-synchronous* circular orbit planet, the daily average stellar insolation on day n is (see Liou (2000))

$$F(\phi, n) = \frac{S}{\pi} \mu(\phi, n) H(\phi, n), \quad (5.1)$$

*non-synchronous means the planet is not in the state of synchronous rotation or tidal locking. Thus the planet does not have permanent day side or night side.

in which ϕ is the latitude, S is the stellar constant, $\mu(\phi, n)$ is the daily average $\cos \theta_z$ (θ_z is the stellar zenith angle), and $H(\phi, n)$ is the half day length (half of the time span from sunrise to sunset) scaled by 2π (24 hours is represented as 2π).

$\mu(\phi, n)$ and $H(\phi, n)$ can be calculated using the following relationships (Vardavas & Taylor (2007)):

$$\mu(\phi, n) = \sin \phi \sin \delta(n) + \cos \phi \cos \delta(n) \frac{\sin H(\phi, n)}{H(\phi, n)}, \quad (5.2)$$

and

$$H(\phi, n) = \arccos[-\tan \phi \tan \delta(n)], \quad (5.3)$$

where

$$\delta(n) = -\varepsilon \cos \frac{2\pi}{N} n \quad (5.4)$$

is the stellar declination angle[†] of day n (Cooper (1969)). Here ε is the planetary obliquity in radians, and $N = T_r/T_s$ (T_r is the revolutionary period, T_s is the spin period) represents the number of days in a year of the planet in consideration.

Special attention should be paid to polar regions where polar day/night could occur over a certain period of a year. If $\tan \phi \tan \delta(n) > 1$, then $H(\phi, n) = \pi$; if $\tan \phi \tan \delta(n) < -1$, then $H(\phi, n) = 0$.

The annual mean insolation at a certain latitude ϕ is:

$$\overline{F(\phi)} = \frac{1}{N} \sum_{n=1}^N F(\phi, n) \quad (5.5)$$

The annual mean zenith angle for a certain latitude ϕ can be obtained by:

$$\overline{\mu(\phi)} = \cos \overline{\theta_z(\phi)} = \frac{\overline{F(\phi)}}{S}. \quad (5.6)$$

It should be particularly noted that the above calculations are based on the assumption that the orbit of the planet is circular rather than elliptical. If the orbit is elliptical with a non-negligible eccentricity, there will be various complicated modifications to the above equations. More orbital factors like the position of equinox points along the orbit, the eccentricity and so on

[†]Stellar declination angle is defined as the angle between the equatorial plane and the line joining the substellar point and the star. For Earth, it varies between -23.44° and 23.44° at present.

will appear in the calculation. It might seem that the position of equinox points is not directly influencing the insolation for a certain latitude, but combining with eccentricity, it determines the insolation difference between the two hemispheres[‡]. For the time being, we only consider circular orbits for simplicity.

5.2 Using ISR as an external forcing of the 1-D R-C model

As shown in Section 5.1, the annual mean incoming stellar radiation (ISR) varies with different latitudes. A Fortran programme is written to calculate the daily average and annual mean ISR at 35 different latitudes ($0^\circ, \pm 5^\circ, \pm 10^\circ, \dots, \pm 85^\circ$) for any circular orbit planet. Various parameters, including mean orbital distance, planetary obliquity, effective temperature of the star, radius of the star, and the number of days in a year can be modified within this programme. Using Earth's parameter settings, the daily ISR at TOA for different latitudes calculated by this programme is shown in Figure 5.1. Note that the northern and southern hemispheres are perfectly symmetric in our calculations of received ISR. But in fact, the Earth's orbit is slightly elliptical, which makes the southern hemisphere receive more insolation since the Earth is closer to the sun near the southern hemisphere summer, thus leading to a small asymmetry between the two hemispheres (cf. Figure 5.2).

Figure 5.3 shows the annual mean ISR at TOA calculated based on daily averages. Since the Earth has a moderate obliquity of 23.44° , the maximum of ISR appears at the equator. As we shall see in the next chapter, if this obliquity goes to values higher than 50° the poles will tend to receive more insolation than the equator, which is the case for Uranus and perhaps some of the exoplanets.

This ISR programme could be further coupled with the 1-D R-C model. The ISR calculated at 35 latitudes by this programme is exported to the 1-D model as an external forcing. The 1-D model is then executed at corresponding latitudes, producing 35 R-C equilibrium temperature profiles. This could lead to the contour map of Figure 5.4.

[‡]For Earth, the change of the position of equinox points in the orbit in geological time scale is known as *axial precession*, which is a major component of the Milankovitch cycles. The physical cause of such orbital 'drift' is the tidal torque exerted by the Sun and the moon.

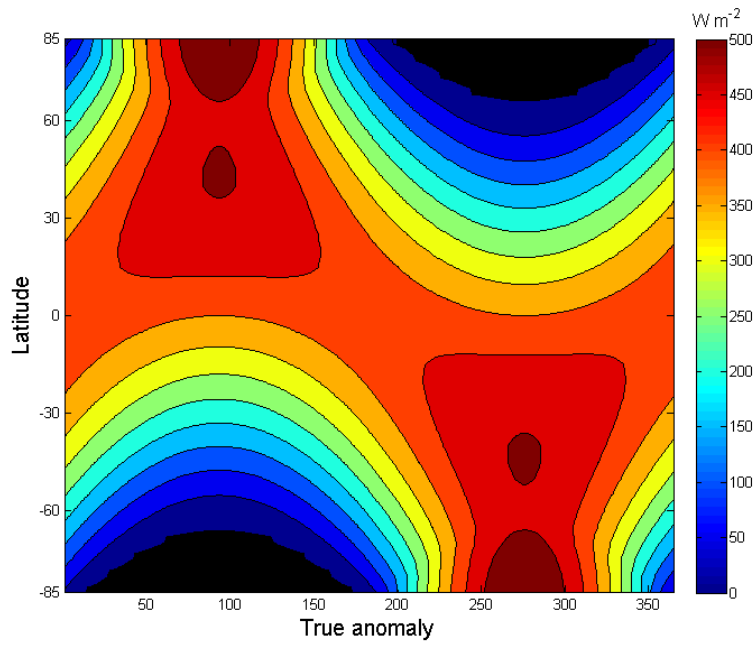


Figure 5.1: Spatial and temporal distribution of daily average ISR at TOA of the Earth. Black regions represent polar night. The abscissa *true anomaly* is the angular difference (in degrees) between the direction of periapsis and the position of the planet, which could be viewed as an indicator of time in one astronomical year.

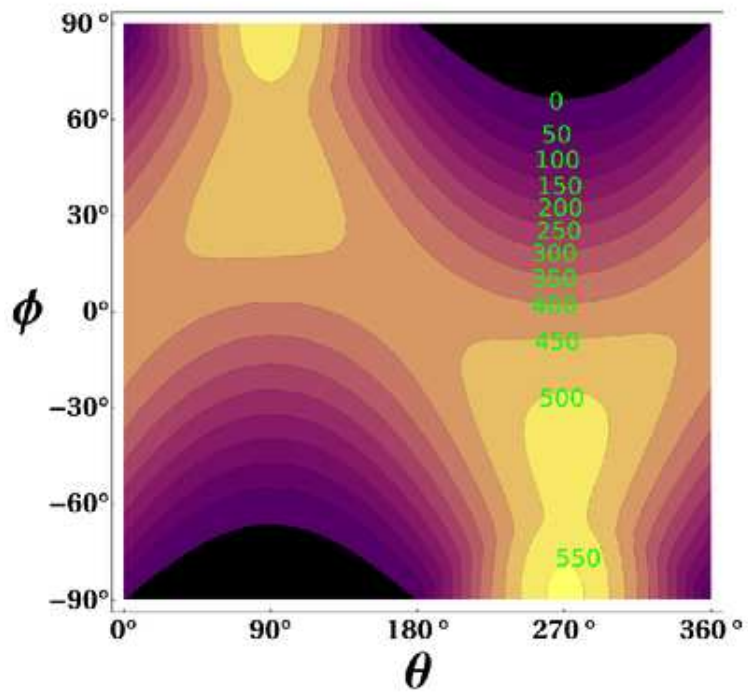


Figure 5.2: Same as Figure 5.1, except that this is calculated by assuming the elliptical orbit of Earth, with eccentricity 0.016704.(see <http://en.wikipedia.org/wiki/Insolation>)

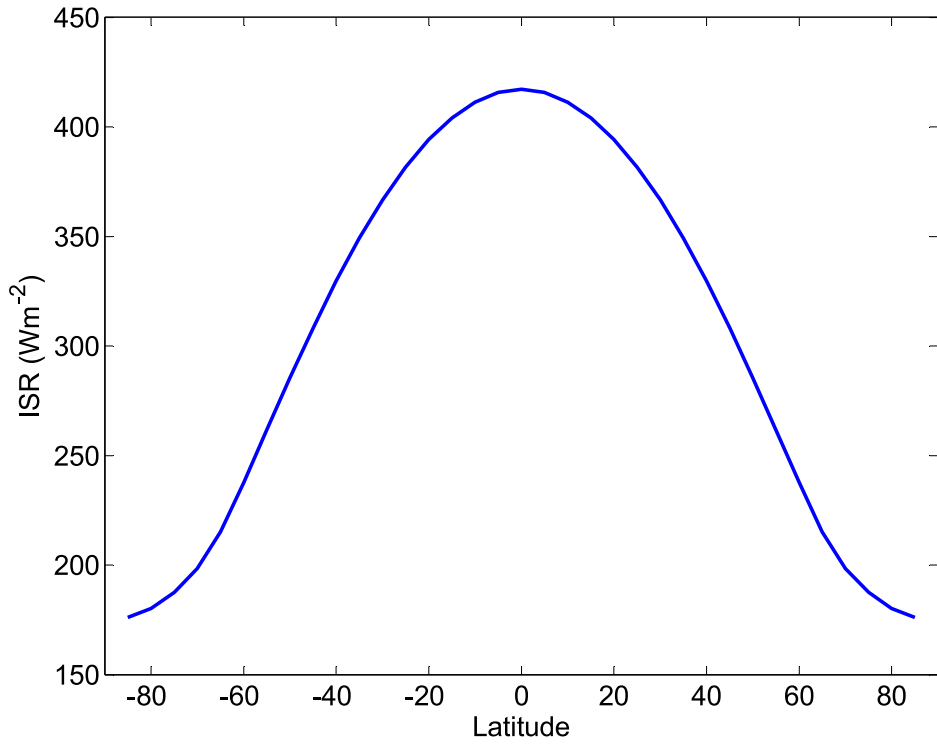


Figure 5.3: Annual mean ISR (in Wm^{-2}) at TOA of the Earth.

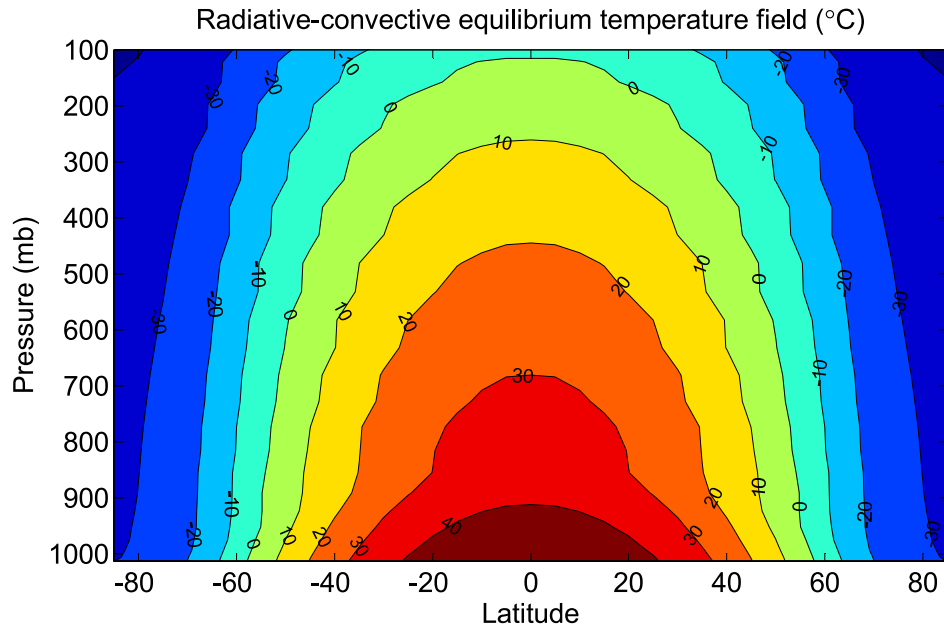


Figure 5.4: Latitude-height map of the radiative-convective equilibrium temperature field within the troposphere generated by the 1-D model running at 35 different latitudes. Calculated with $k_{sw}^* = 0.00019 \text{ cm}^2 \text{ g}^{-1}$, $k_{lw}^* = 0.001 \text{ cm}^2 \text{ g}^{-1}$,

As we can see in this latitude-height cross-section plot, the surface R-C equilibrium temperature difference between the equator and the poles is roughly $80K$, which is obviously larger than what we observe in the real terrestrial atmosphere. An important caveat for this map is that we followed the assumption made for the 1-D model—that the short-wave absorbers spread uniformly in the vertical direction. Therefore, ozone in Earth’s atmosphere essentially spreads evenly across the whole atmospheric column in our model. That makes this map differ considerably from the real R-C equilibrium temperature field in various respects. Nevertheless, the basic pattern of the R-C equilibrium temperature distribution is clearly reflected and the R-C equilibrium surface temperature difference is estimated relatively accurately (the radiative equilibrium equator-to-pole temperature difference is roughly $80 K$, see Schneider (2006), Held & Hou (1980)).

Chapter 6

Glimpse of the Radiative Parameter Space

The 1-D model described in the last two chapters has a range of parameters available to be varied within a multiple dimensional parameter space. This chapter presents our preliminary explorations of the parameter space constructed by some of the suitably non-dimensional radiative parameters of the 1-D model. By varying the values of planetary obliquity, ratio of long-wave to short-wave optical depth, as well as the absolute value of long-wave optical depth, clear trends could be found among the various thermal structures obtained.

6.1 Choose of parameters

At least 9 parameters in our semi-grey R-C model could be modified by the experimenter: surface pressure p_s , long-wave total optical depth of the atmosphere τ_{lw} , short-wave total optical depth τ_{sw} , planetary bond albedo A , stellar constant S_0 at the mean distance between the parent star and the planet, the gravitational acceleration g , the specific heat capacity at constant pressure c_p , the planetary obliquity ε , the number of days N within an orbital period. A reasonable first step towards constructing the characteristic dimensionless parameters from these quantities is to pick up those quantities that are nondimensional by definition. Among these parameters, A , N , τ_{lw} , τ_{sw} , ε can be viewed as nondimensional. But the influence of A could be combined into the modification of S_0 , and the effect of N is only important when it is fairly small (e.g. for tidally-locked planets). If we consider the non-synchronously rotating planets only, then A and N will

not be the independent defining parameters. Similarly, the effect of p_s can be combined with τ_{lw} and τ_{sw} . This leaves only τ_{lw} , τ_{sw} , and ε as the characterising dimensionless parameters. In this chapter, we choose τ_{lw}/τ_{sw} , ε , and τ_{lw} to be the nondimensional characteristic parameters. The reason we use τ_{lw}/τ_{sw} is that this parameter acts as an index of greenhouse or anti-greenhouse effect which will be discussed in more details in Section 6.2.

6.2 Sensitivity of global average thermal structure

In order to study the model atmosphere's sensitivity to its optical properties, we ran a series of experiments of varying both τ_{lw}/τ_{sw} and the absolute value of τ_{lw} using the 1-D R-C model described in Chapter 3. Three different ratios $\tau_{lw}/\tau_{sw} = 5/1, 1/1, 1/5$ and two different absolute values $\tau_{lw}^* = 2, 20$ are tested, which together make 6 different combinations. For experiments of optically thick atmospheres with $\tau_{lw}^* = 20.0$, 100 vertical layers are used rather than the standard setting of 40. In practice, the change of the absolute value of τ_{lw}^* is done by changing the surface pressure p_s . Thus, $\tau_{lw}^* = 2$ corresponds to $p_s = 1013.25 \text{ mb}$, whereas $\tau_{lw}^* = 20$ corresponds to $p_s = 10132.5 \text{ mb}$. The ratio of τ_{lw}^*/τ_{sw}^* is changed in the model by modifying the values of scaled extinction coefficients k_{lw}^* and k_{sw}^* .

Figure 6.1 shows the 1-D vertical temperature profiles representing the globally averaged conditions of the 6 experiments grouped into 3 plots. Within each plot, there are significant overlaps between the two curves, which represent the optically thin and optically thick cases respectively. For $\tau_{lw}^* = 5/1$ (left panel), the blue curve shows the terrestrial profile (with parameter setting: $k_{lw}^* = 0.001 \text{ cm}^2\text{g}^{-1}$, $k_{sw}^* = 0.0002 \text{ cm}^2\text{g}^{-1}$, and $p_s = 1013.25 \text{ mb}$). The optically thick curve (red one) with this ratio follows the terrestrial profile above 1 bar level and extends sub-adiabatically to a surface temperature of roughly 370 K . This is qualitatively similar to the thermal structure of Venus, which could be viewed as a further extended curve reaching a surface temperature of about 730 K (see Figure 6.2).

The fundamental character of the profiles in the left panel is that it is warmer in the lower atmosphere and cooler in the upper part, a phenomenon related to the *greenhouse effect*, which warms up the planetary surface as well as the lower atmosphere. Short-wave stellar radiation could penetrate the atmosphere without much extinction whereas the long-wave thermal radiation emitted by the planetary surface and atmosphere are greatly absorbed and scattered within the atmosphere. The atmosphere thus acts like

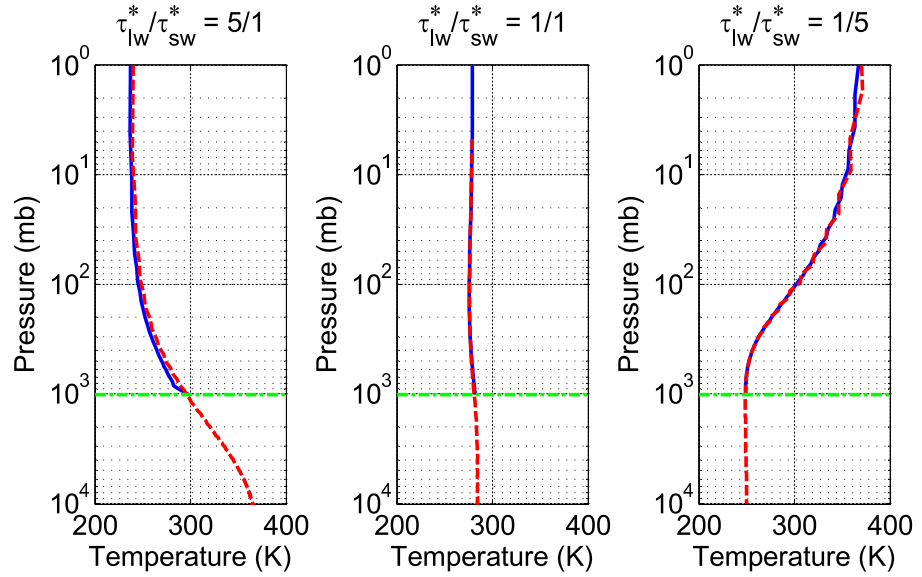


Figure 6.1: Vertical temperature profiles of the optically thin ($\tau_{lw}^* = 2$) and optically thick ($\tau_{lw}^* = 20$) atmospheres with $\tau_{lw}^* / \tau_{sw}^* = 5/1, 1/1, 1/5$ respectively. Blue curves represent optically thin atmospheres while red curves represent optically thick atmospheres. Green dash dot lines represent the ground level ($101325 Pa$) for optically thin atmospheres. Stellar constant is set to the solar constant for Earth’s mean orbit.

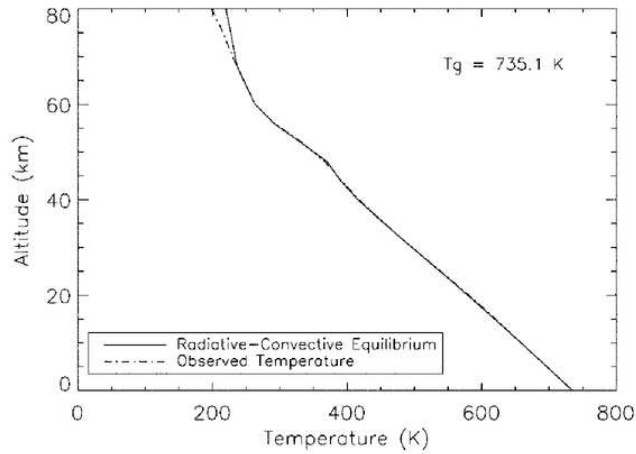


Figure 6.2: Dash line represents the vertical temperature profile of VIRA (Venus International Reference Atmosphere). Solid line represents the profile calculated by a radiative model. From Bullock & Grinspoon (2001)

a greenhouse* which blocks the heat transferred by long-wave radiation but allows the short-wave radiation to freely reach the surface. The atmosphere could thus be regarded as being heated from below by the ground rather than from above by the star. This pattern of warm air lying beneath cold air could be found on Solar System planets like Venus, Earth and Mars, albeit there is an inversion layer on Earth due to the short-wave absorption effect of ozone.

An inverse pattern to this with warm air lying over cool air is mainly caused by the so-called *anti-greenhouse* effect, which could be appreciated in the right panel of Figure 6.1. In the case shown here, the atmosphere is fairly opaque to the short-wave stellar radiation yet relatively transparent to the long-wave thermal radiation. Therefore, downward-going stellar radiation will be significantly absorbed and extinguished before reaching the surface, whereas the long-wave radiation emitted by the atmosphere and planetary surface could escape comparatively easily towards the space. The atmosphere could be viewed as being heated directly by the parent star from above, in contrast with the more familiar ground heated atmosphere we enjoy on the Earth.

Titan's atmosphere (see Figure 6.3) is usually referred to as an example of the anti-greenhouse effect in the Solar System (see the discussions of McKay et al. (1991)). The warm region in the middle level of Titan's atmosphere is in fact caused by the localised heating of sunlight-absorbing organic hazes, which somewhat resemble the effect of ozone in Earth's stratosphere. But the hazes on Titan are dramatically more efficient than Earth's ozone layer at absorbing solar radiation (90% of UV and visible solar radiation is absorbed by this organic haze layer on Titan). Besides, this haze layer is very inefficient at trapping the infrared radiation, thus creating a local anti-greenhouse effect that leads to the temperature inversion in Titan's middle atmosphere. The lower atmosphere however, is not forced by anti-greenhouse effect due to the lack of hazes. The remaining solar radiation warms up the surface which in turn forces convection and weather processes in an Earth-like troposphere (see Figure 6.3).

More general anti-greenhouse effects, which span across the vertical extent of the atmosphere rather than being locally confined within some layers, are possible on certain rocky exoplanets orbiting M-dwarf stars (Hu & Ding (2011)). M-dwarf stars are main sequence stars with smaller mass and cooler

*There are fundamental differences, however, between the mechanism of a real greenhouse and the atmosphere we mentioned here. A real greenhouse does not increase the temperature within it by adjusting the radiative balance. Instead its glass wall stops the heat transfer assumed by air motions, thus warms up its internal environment.

surface temperature than our Sun. These small, dim M-dwarfs constitute the vast majority of stars in the universe. According to stellar evolution theories (Prialnik (2000)), smaller stars tend to have a longer lifespan, thus M-dwarfs are thought to be able to provide a relatively longlasting environment for life or even civilisation to evolve around it (Irwin et al. (2009)). In fact, there has been a series of planets discovered orbiting around M-dwarfs (e.g. the Gliese 581 system) with potentially habitable climates (Wordsworth et al. (2011), Hu & Ding (2011), Selsis et al. (2007)). For an M-dwarf star with much cooler temperature than the Sun, its radiative spectrum peaks at longer wavelength regions rather than in the visible band. For example, Gliese 581 is observed to have a surface temperature of 3200 K (Udry et al. (2007)). According to Wien’s displacement law, the blackbody spectrum at such a temperature peaks at about $0.9\ \mu\text{m}$, which is in near infrared band. If a planet orbiting this star has an atmosphere made of CO_2 or H_2O , it will absorb strongly the stellar radiation, which cools the surface and warms up the upper atmosphere. If such a planet lies closely enough to the parent star that the atmospheric temperature is comparable to the effective temperature of the star, then the spectra of the stellar radiation and the planetary thermal radiation will largely overlap. The resulting thermal structure will qualitatively resemble the middle panel of Figure 6.1, which shows an atmosphere with same extinction coefficient at the long-wave and short-wave bands. In this case, there will be no greenhouse or anti-greenhouse effect, thus leading to a roughly isothermal atmosphere in the vertical direction.

6.3 Sensitivity of the equator-to-pole temperature difference

In the previous section, we discussed the dependence of the globally averaged thermal structures on the radiative properties of planetary atmospheres. When it comes to the latitudinal variations of the temperature field, the influence of planetary obliquity must be considered. Figure 6.4 shows the annual mean ISR at TOA for three obliquities: 23.44° , 50.00° , and 75.00° respectively. As we can see, for small obliquity angle, like the Earth’s current value 23.44° , the ISR peaks over the equator and has minimum values at the poles. For very large obliquity angle (75.00° in our experiment, Uranus has an obliquity of 97.77°), the poles will receive the maximum amount of ISR while the equator receives the least. The transition from peaking at equator to peaking at the poles occurs near $\varepsilon = 50^\circ$ in our model. The green curve in Figure 6.4 represents the ISR at TOA for obliquity of 50.00° , which shows

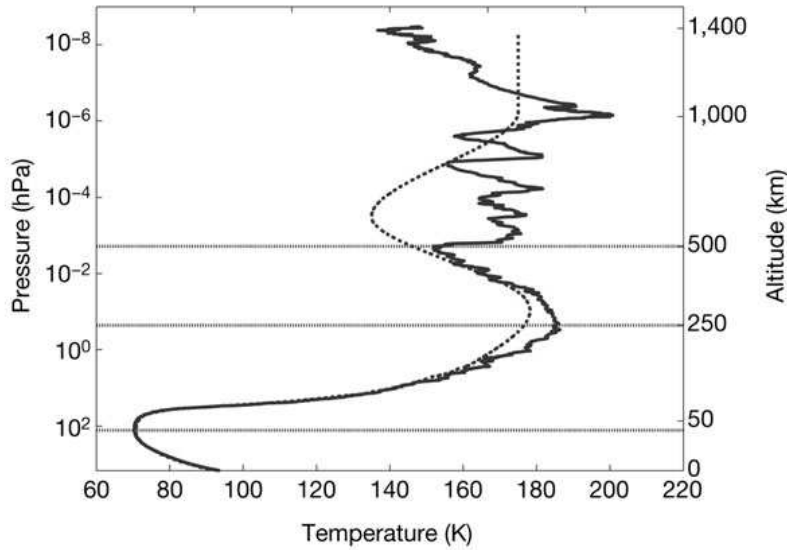


Figure 6.3: Observed vertical temperature profile of Titan by the Huygens probe. Dash line represents the profile estimated by an numerical model. (From Fulchignoni et al. (2005))

very little variation in the meridional direction.

This pattern of ISR distribution in the meridional direction indicates that similar temperature distribution should be observed within the atmosphere. This can be inferred from Table 6.1 and Table 6.2 where the R-C equilibrium equator-to-pole temperature differences under various different conditions are shown. Table 6.1 shows experiments done with $\tau_{lw}^* = 2.0$ which corresponds to Earth's long-wave optical depth, while Table 6.2 shows experiments with $\tau_{lw}^* = 20.0$ which is 10 times thicker. Within each table, three obliquities and three optical depth ratios give 9 different combinations. The influence of planetary obliquity could be easily found by comparing rows within each table. The temperature difference for obliquity 50.00° is in the order of 1 K , which is in consistent with the relatively uniform distribution of incoming stellar radiation. Earth's obliquity leads to a significant equator-to-pole temperature difference. For optical depth ratio of $5/1$ and τ_{lw}^* (which are the values of Earth), the R-C equilibrium temperature difference could be 81 K (cf. Figure 5.4).

Another clear trend in these two tables is that the equator-to-pole temperature difference increases as the optical depth ratio τ_{lw}^*/τ_{sw}^* increases (compare the columns in each table). The differences between columns in

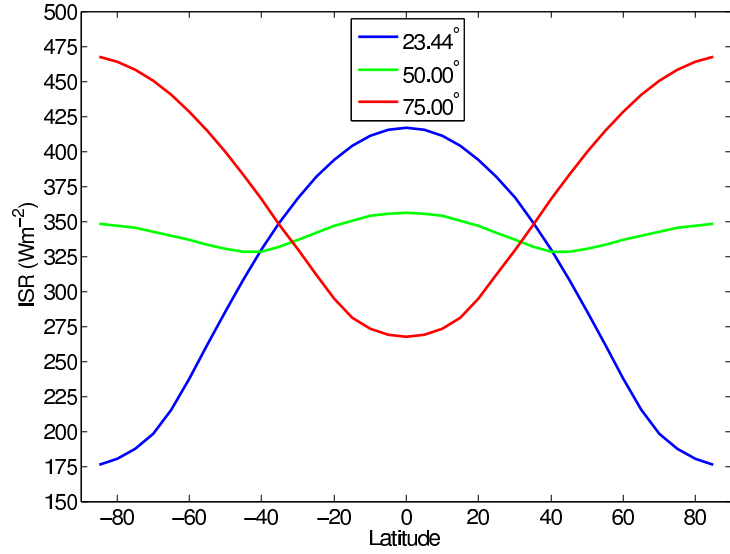


Figure 6.4: ISR at TOA at different latitudes for three different obliquities. The blue curve represents the scenario of present-day Earth, with obliquity of 23.44° . The red curve represents the Earth with a rather large obliquity angle of 75° , somewhat resembling Uranus. The green curve stands for an intermediate state with obliquity 50° .

Obliquity	τ_{lw}^*/τ_{sw}^*		
	1/5	1/1	5/1
23.44°	43K	67K	81K
50.00°	1.5K	2K	2.1K
75.00°	-33K	-50K	-54K

Table 6.1: Equator-to-pole temperature difference ΔT_h at the planetary surface for different obliquity angles and different τ_{lw}^*/τ_{sw}^* . $\tau_{lw}^* = 2.0$ for all these experiments.

Obliquity	τ_{lw}^*/τ_{sw}^*		
	1/5	1/1	5/1
23.44°	35K	47K	65K
50.00°	0.9K	1K	1.2K
75.00°	-20K	-31K	-33K

Table 6.2: Same as Table 6.1 except $\tau_{lw}^* = 20.0$ for all these experiments.

each table is the value of short-wave optical depth τ_{sw}^* . It could thus be inferred that the more transparent the atmosphere is to stellar radiation, the larger ΔT_h will be. Besides, comparison between Table 6.1 and Table 6.2 shows that optically thicker atmospheres tend to have smaller temperature differences. These trends, combined with the dependence of ΔT_h on planetary obliquity ε , imply a possibility of parameterising ΔT_h in terms of the three parameters τ_{lw}^*/τ_{sw}^* , τ_{lw}^* , and ε (see the discussions in Chapter 7).

Chapter 7

Conclusions and Future Work

7.1 Major conclusions

This report presents the work done within my second year focusing on the construction of a 1-D semi-grey R-C model and its application to explore the parameter space constructed by three radiative parameters. The model has two bands representing short-wave stellar radiation and long-wave planetary thermal radiation respectively, and constant extinction coefficient is assigned to each band. The convective adjustment scheme by Manabe & Wetherald (1967) is coupled with the radiative transfer scheme to prevent the atmosphere from developing statically unstable stratification. Such simplified dual-band scheme, although neglects various detailed radiative processes, captures essentially the key physics of radiative transfer and the corresponding diabatic heating. The model is validated in the context of classical grey atmosphere against analytical results, and is tuned to model the terrestrial and Martian atmospheres, which shows encouraging results. The model is proved to be able to emulate the fundamental vertical thermal structures that are common to rocky planetary atmospheres, albeit more peculiar features, especially those associated with the inhomogeneous distribution of absorbers, are difficult to be reproduced in our 1-D model. A programme calculating the incoming stellar radiation at top of atmosphere is developed and coupled with the 1-D model so that it could represent the latitudinal variations of the atmospheric temperature field. This basically means forcing the 1-D model with annual-mean incoming stellar radiation and annual-mean stellar zenith angle at corresponding latitudes.

Various thermal structures are obtained by varying the values of three parameters (τ_{lw}^*/τ_{sw}^* , ε , and τ_{lw}^*). Three distinctive patterns of temperature profiles are obtained by varying the ratio of τ_{lw}^*/τ_{sw}^* . Greenhouse and anti-greenhouse effects are investigated by comparing the profiles of different τ_{lw}^*/τ_{sw}^* with the observed profiles of Venus and Titan. Clear trends are also found when varying the planetary obliquity to three values: 23.44° , 50.00° , and 75.00° . For the small obliquity angle like the terrestrial value 23.44° , the incoming stellar radiation peaks at the equatorial region and the poles receive minimum amount of stellar radiation. This leads to a temperature field that is warm at lower latitudes and cold at higher latitudes. For the intermediate obliquity angle 50.00° , the latitudinal difference of received ISR is very small. Therefore the equator-to-pole temperature difference for 50.00° obliquity is in order of 1 K . For even greater obliquity angle, like 75.00° , the poles receive more ISR than the equator, and the temperature field is then featured by lower temperature at tropics and higher temperature at polar regions. Comparison of the R-C equilibrium equator-to-pole temperature difference obtained by varying values of τ_{lw}^*/τ_{sw}^* , ε , and τ_{lw}^* shows clear dependences of ΔT_h on these three dimensionless parameters, which implies a possible parameterisation scheme to estimate ΔT_h in terms of them, albeit other parameters like planetary rotation rate will perhaps also appear in the ultimate parameterisation expression.

7.2 Discussions and future plan

7.2.1 Dimensionless parameters

The ultimate goal of this project is to use several characteristic dimensionless parameters to establish a parameter space in which various circulation regimes are mapped and classified. In Chapter 1, we have mentioned at least three dimensionless parameters to define the planetary circulation regimes: Thermal Rossby number $\mathcal{R}o$, the radiative damping parameter \mathcal{F}_r , and the frictional damping parameter \mathcal{F}_f . After introducing the semi-grey R-C scheme to replace the Newtonian cooling scheme used by PUMA in my first year, more radiation-related parameters needs to be included in our parameter space. The following parameters are intuitively thought to be of importance in characterising the planetary thermal structure and hence the circulation patterns: ratio of long-wave to short-wave optical depth (τ_{lw}^*/τ_{sw}^*), absolute value of long-wave optical depth (τ_{lw}^*), planetary obliquity (ε), stellar constant at the planet's mean orbital distance (S_0), and the ratio of radiative timescale to advective timescale (τ_r/τ_a).

The first three parameters (τ_{lw}^*/τ_{sw}^* , τ_{lw}^* , ε) listed above have been investigated in Chapter 6. The stellar constant S_0 determines the amount of radiation received by the planet*. The ratio τ_r/τ_a determines whether the radiative equilibrium temperature field could stay under the influence of dynamical disturbances. If this ratio is smaller than 1, then the real temperature field will probably not differ too much from the R-C equilibrium field predicted using the R-C model described in this report. Radiative timescale τ_r could be estimated by (Showman et al. (2010), James (1994)):

$$\tau_r \sim \frac{c_p p_s}{4\sigma T_e^3 g}, \quad (7.1)$$

where c_p is the specific heat capacity at constant pressure, p_s is the surface pressure, σ is the Stefan-Boltzmann constant, T_e is the effective blackbody temperature of the planet which is determined by stellar radiation and planetary bond albedo, g is the gravitational acceleration.

Advective timescale could be estimated by:

$$\tau_a \sim \frac{a}{U}, \quad (7.2)$$

where U could be estimated by the characteristic thermal wind $U = \frac{R\Delta\theta_h}{\Omega a}$.

These parameters together will lead to a parameter space with 8 dimensions ($\mathcal{R}o$, \mathcal{F}_r , \mathcal{F}_f , τ_{lw}^*/τ_{sw}^* , τ_{lw}^* , ε , S_0 , τ_r/τ_a), which will be computationally very expensive. Besides, S_0 here is a parameter with dimension. It is therefore convenient if we combine some of them so that the total number of parameters could be reduced. Many of the radiative parameters we introduced here can be related to the determination of the observed $\Delta\theta_h$ that appear in the definition of $\mathcal{R}o$. If we could find out an estimation of $\Delta\theta_h$ in terms of these parameters, we could combine their effect into a single parameter $\mathcal{R}o$ and dramatically decrease the dimension of the parameter space.

7.2.2 $\Delta\theta_h$ parametrisation revisited

Various parametrisation schemes have been discussed in Chapter 1. Those schemes usually stems from analytical derivations based on various assumptions (baroclinic adjustment by Stone (1978) is a typical example). Another perhaps more relevant approach for our current situation is to start from

*We include the effect of planetary bond albedo A into the value of S_0 . Thus it should be viewed as a modified stellar constant $S_0 \times (1 - A)$.

dimensional considerations and parameterise $\Delta\theta_h$ in terms of radiative and thermodynamic parameters. Golitsyn (1970) took this approach combined with some assumptions about the atmospheric energetics and came up with a parametrisation of ΔT_h in this form:

$$\Delta T_h \sim \frac{(S_0/4)^{9/16}}{\sigma^{1/16} c_p^{3/4}} \sqrt{\frac{ag}{p_s}}, \quad (7.3)$$

where a is planetary radius.

In this parametrisation scheme, the effect of S_0 is reflected, and the effect of τ_{lw}^* is partly reflected since τ_{lw}^* is proportional to p_s . If we follow this approach and further include τ_{lw}^*/τ_{sw}^* and ε into this scheme, then the defining parameters will be reduced to the following: $\mathcal{R}o$, \mathcal{F}_r , \mathcal{F}_f , τ_r/τ_a . Note that the effect of the radiative damping parameter $\mathcal{F}_r = 4\pi\tau_r^2$ can be reflected in τ_r/τ_a . Therefore this list can be further reduced to only 3 parameters: $\mathcal{R}o$, \mathcal{F}_f and τ_r/τ_a ! This will greatly alleviate the computational burden of conducting large ensemble numerical experiments. If we test 5 different values for each parameter, this gives $5^3 = 125$ experiments to run, in contrast with the $5^8 = 390625$ experiments to run if there are 8 parameters as we mentioned above. More importantly, if the parametrisation scheme is reasonable and accurate enough, this approach will provide a way of estimating $\Delta\theta_h$ and therefore $\mathcal{R}o$ in terms of external parameters only, thus solving the problem of making $\mathcal{R}o$ an external parameter that we mentioned in Chapter 1. The ultimate parameter space will therefore be constructed by $\mathcal{R}o$, \mathcal{F}_f and τ_r/τ_a .

7.2.3 Time plan

- Oct—Dec 2011
 - Generalise the ISR calculation programme to planets in elliptical orbits.
 - Couple the 1-D R-C scheme to the 2-D PUMA, replacing the Newtonian cooling scheme.
- Jan—Mar 2012
 - Use the new 3-D PUMA to run the experiments of varying rotation rates.
 - Design and test parametrisation schemes of $\Delta\theta_h$.
- Apr—Jun 2012

- Run the ensemble experiments by changing values of the three dimensionless parameters.
 - Diagnose the results of the experiments (e.g. zonal mean temperature field, Hadley cell extent and intensity, jet stream distribution and intensity, dominant instability mechanism, deformation radius and so on).
- Jul—Sep 2013
 - Write up the thesis.

Bibliography

- Andrews, D.G. (2010) *An Introduction to Atmospheric Physics*. Cambridge University Press, second ed.
- Barry, L., G. C. Craig, & J. Thurnburn (2002) Poleward heat transport by the atmospheric heat engine. *Nature* **415**: 774–777.
- Batchelor, G.K. (2000) *An Introduction to Fluid Dynamics*. Cambridge University Press, new ed.
- Bjerknes, J. (1919) On the structure of moving cyclones. *Monthly Weather Review* **47**: 95–99.
- Bullock, M. A. & D. H. Grinspoon (2001) The Recent Evolution of Climate on Venus. *Icarus* **150**: 19–37.
- Charney, J. G. (1947) The Dynamics of Long Waves in a Baroclinic Westerly Current. *Journal of Atmospheric Sciences* **4**: 136–162.
- Cooper, P. I. (1969) The absorption of radiation in solar stills. *Solar Energy* **12**: 333–346.
- Crisp, D. (1989) Radiative forcing of the Venus mesosphere. II - Thermal fluxes, cooling rates, and radiative equilibrium temperatures. *Icarus* **77**: 391–413.
- Del Genio, A. D. & R. J. Suozzo (1987) A comparative study of rapidly and slowly rotating dynamical regimes in a terrestrial general circulation model. *Journal of Atmospheric Sciences* **44**: 973–986.
- Emanuel, K.A. (1994) *Atmospheric Convection*. Oxford University Press.
- Ferrel, W. (1889) *A popular treatise on the winds*. New York, Wiley.

- Fleming, E. L., S. Chandra, J. J. Barnett, & M. Corney (1990) Zonal mean temperature, pressure, zonal wind and geopotential height as functions of latitude. *Advances in Space Research* **10**: 11–59.
- Fulchignoni, M., F. Ferri, F. Angrilli, A. J. Ball, A. Bar-Nun, M. A. Barucci, C. Bettanini, G. Bianchini, W. Borucki, G. Colombatti, M. Coradini, A. Coustenis, S. Debei, P. Falkner, G. Fanti, E. Flamini, V. Gaborit, R. Grard, M. Hamelin, A. M. Harri, B. Hathi, I. Jernej, M. R. Leese, A. Lehto, P. F. Lion Stoppato, J. J. López-Moreno, T. Mäkinen, J. A. M. McDonnell, C. P. McKay, G. Molina-Cuberos, F. M. Neubauer, V. Pirronello, R. Rodrigo, B. Saggin, K. Schwingenschuh, A. Seiff, F. Simões, H. Svedhem, T. Tokano, M. C. Towner, R. Trautner, P. Withers, & J. C. Zarnecki (2005) In situ measurements of the physical characteristics of Titan’s environment. *Nature* **438**: 785–791.
- Fultz, D., R.R. Long, G.V. Owens, W. Bowen, R. Kaylor, & J. Weil (1959) Studies of thermal convection in a rotating cylinder with some implications for large-scale atmospheric motions. *Meteorological Monographs American Meteorological Society* **4**.
- Geisler, J. E., E. J. Pitcher, & R. C. Malone (1983) Rotating-Fluid experiments with an atmospheric general circulation model. *Journal of Geophysical Research* **88**: 9706–9716.
- Golitsyn, G. S. (1970) A Similarity Approach to the General Circulation of Planetary Atmospheres. *Icarus* **13**: 1–24.
- Goody, R.M. & Y.L. Yung (1989) *Atmospheric Radiation: Theoretical Basis*. Oxford University Press.
- Green, J. S. A. (1970) Transfer properties of the large-scale eddies and the general circulation of the atmosphere. *Quarterly Journal of the Royal Meteorological Society* **96**: 157–185.
- Hadley, G. (1735) Concerning the Cause of the General Trade-Winds: By Geo. Hadley, Esq; F. R. S. *Royal Society of London Philosophical Transactions Series I* **39**: 58–62.
- Held, I. M. (1999) The macroturbulence of the troposphere. *Tellus Series A* **51**: 59–70.
- Held, I. M. & A. Y. Hou (1980) Nonlinear Axially Symmetric Circulations in a Nearly Inviscid Atmosphere. *Journal of Atmospheric Sciences* **37**: 515–533.

- Held, I. M. & V. D. Larichev (1996) A Scaling Theory for Horizontally Homogeneous, Baroclinically Unstable Flow on a Beta Plane. *Journal of Atmospheric Sciences* **53**: 946–952.
- Heng, K., D. M. W. Frierson, & P. J. Phillipps (2011) Atmospheric circulation of tidally locked exoplanets II: dual-band radiative transfer and convective adjustment. *ArXiv e-prints* .
- Hide, R. (1953) Some experiments on thermal convection in a rotating liquid. *Quarterly Journal of the Royal Meteorological Society* **79**: 161–161.
- Hide, R. (1969) *Some laboratory experiments on free thermal convection in a rotating fluid subject to a horizontal temperature gradient and their relation to the theory of the global atmospheric circulation.*In: Corby, G.A.(Ed.), *The Global Circulation of the Atmosphere*. Royal Meteorological Society, London.
- Hide, R. (2010) A path of discovery in geo physical fluid dynamics. *Astronomy and Geophysics* **51**(4): 040000–4.
- Hide, R. & P. J. Mason (1975) Sloping convection in a rotating fluid. *Advances in Physics* **24**: 47–100.
- Houghton, J. (2002) *Physics of Atmospheres*. Cambridge University Press, third ed.
- Hu, Y. & F. Ding (2011) Radiative constraints on the habitability of exoplanets Gliese 581c and Gliese 581d. *Astronomy and Astrophysics* **526**.
- Hunt, B. G. (1979) The Influence of the Earth’s Rotation Rate on the General Circulation of the Atmosphere. *Journal of Atmospheric Sciences* **36**: 1392–1408.
- Irwin, J., D. Charbonneau, P. Nutzman, & E. Falco (2009) The MEarth project: searching for transiting habitable super-Earths around nearby M dwarfs. In *IAU Symposium, IAU Symposium*, vol. 253, 37–43.
- James, I.N. (1994) *Introduction to Circulating Atmospheres*. Cambridge University Press, UK.
- Lacis, A. A. & V. Oinas (1991) A description of the correlated-k distribution method for modelling nongray gaseous absorption, thermal emission, and multiple scattering in vertically inhomogeneous atmospheres. *Journal of Geophysical Research* **96**: 9027–9064.

- Liou, K.N. (2000) *An Introduction to Atmospheric Radiation*. Academic Press, second ed.
- Lorenz, E.N. (1969) *The Nature and Theory of the General Circulation of the Atmosphere*. No.218.W.M.O.,Geneva.
- Manabe, S. & R. F. Strickler (1964) Thermal Equilibrium of the Atmosphere with a Convective Adjustment. *Journal of Atmospheric Sciences* **21**: 361–385.
- Manabe, S. & R. T. Wetherald (1967) Thermal Equilibrium of the Atmosphere with a Given Distribution of Relative Humidity. *Journal of Atmospheric Sciences* **24**: 241–259.
- McGuffie, K. & A. Henderson-Sellers (2005) *A Climate Modelling Primer*. John Wiley and Sons, third ed.
- McKay, C. P., J. B. Pollack, & R. Courtin (1991) The greenhouse and antigreenhouse effects on Titan. *Science* **253**: 1118–1121.
- Prialnik, D. (2000) *An Introduction to the Theory of Stellar Structure and Evolution*. Cambridge University Press.
- Ramanathan, V., R. J. Cicerone, J. T. Kiehl, & H. B. Singh (1985) Trace gas trends and their potential role in climate change. *Journal of Geophysical Research* **90**: 5547–5566.
- Read, P. L. (2011) Dynamics and circulation regimes of terrestrial planets. *Planetary and Space Science* **59**: 900–914.
- Read, P.L. & S.R. Lewis (2004) *The Martian Climate Revisited: Atmosphere and Environment of a Desert Planet*. Springer-Praxis.
- Rhines, P. B. (1975) Waves and turbulence on a beta-plane. *Journal of Fluid Mechanics* **69**: 417–443.
- Rossby, C-G. (1939) Relation between variations in the intensity of the zonal circulation of the atmosphere and the displacements of the semi-permanent centers of action. *Journal of Marine Research* **2**: 38–55.
- Satoh, M. (2004) *Atmospheric circulation dynamics and general circulation models*. Springer.
- Schneider, T. (2006) The General Circulation of the Atmosphere. *Annual Review of Earth and Planetary Sciences* **34**: 655–688.

- Selsis, F., J. F. Kasting, B. Levrard, J. Paillet, I. Ribas, & X. Delfosse (2007) Habitable planets around the star Gliese 581? *Astronomy and Astrophysics* **476**: 1373–1387.
- Showman, A.P., J.Y.-K. Cho, & K. Menou (2010) *Atmospheric circulation of exoplanets*, In: Seager, S. (Ed.), *Exoplanets*. University of Arizona Press, Tucson, Arizona.
- Smith, M. D. (2008) Spacecraft Observations of the Martian Atmosphere. *Annual Review of Earth and Planetary Sciences* **36**: 191–219.
- Stone, P. H. (1972) A simplified radiative-dynamical model for the static stability of rotating atmospheres. *Journal of Atmospheric Sciences* **29**: 405–418.
- Stone, P. H. (1978) Baroclinic Adjustment. *Journal of Atmospheric Sciences* **35**: 561–571.
- Taylor, F.W. (2010) *Planetary Atmospheres*. Oxford University Press.
- Thomson, J. (1892) On the grand currents of atmospheric circulation. *Phil. Trans. Roy. Soc.* **183**: 653–684.
- Udry, S., X. Bonfils, X. Delfosse, T. Forveille, M. Mayor, C. Perrier, F. Bouchy, C. Lovis, F. Pepe, D. Queloz, & J.-L. Bertaux (2007) The HARPS search for southern extra-solar planets. XI. Super-Earths (5 and 8 M_{\oplus}) in a 3-planet system. *Astronomy and Astrophysics* **469**: L43–L47.
- Vardavas, I.M. & F.W. Taylor (2007) *Radiation and Climate*. Oxford University Press.
- Weaver, C. P. & V. Ramanathan (1995) Deductions from a simple climate model: Factors governing surface temperature and atmospheric thermal structure. *Journal of Geophysical Research* **1001**: 11585–11592.
- White, A. (2010) The atmosphere, the annulus and quasi-geostrophic theory. *Astronomy and Geophysics* **51**(4): 040000–4.
- Williams, G. P. (1988a) The dynamical range of global circulations I. *Climate Dynamics* **2**: 205–260.
- Williams, G. P. (1988b) The dynamical range of global circulations II. *Climate Dynamics* **3**: 45–84.

Williams, G. P. & J. L. Holloway (1982) The range and unity of planetary circulations. *Nature* **297**: 295–299.

Wordsworth, R. D., F. Forget, F. Selsis, E. Millour, B. Charnay, & J.-B. Madeleine (2011) Gliese 581d is the First Discovered Terrestrial-mass Exoplanet in the Habitable Zone. *The Astrophysical Journal Letters* **733**: L48+.